

ALMA MATER STUDIORUM · UNIVERSITÀ DI BOLOGNA

Scuola di Scienze
Corso di Laurea Magistrale in Fisica del Sistema Terra

Ocean climate predictability study in the Mediterranean Sea

Relatrice:
Prof.ssa Nadia Pinardi

Presentata da:
Roberta Benincasa

Correlatori:
Dott. Giovanni Liguori
Prof. Hans von Storch

Sessione V
Anno Accademico 2021/2022

RIASSUNTO

I modelli numerici oceanici soggetti al forzante atmosferico sono caratterizzati da 2 tipi di variabilità: una risposta al forzante esterno (definito *segnale*) e le variazioni interne generate indipendentemente da esso (che costituiscono il *rumore*). Partendo dalla teoria dei *modelli climatici stocastici* (Hasselmann, 1976) e basandosi su un ensemble di 5 simulazioni del Mar Mediterraneo nel 2021 con lo stesso forzante atmosferico, ma con date di inizio distanziate di un anno, il rumore o variabilità interna è studiata relativamente alla sua dipendenza dalla profondità e dalla stagione, alla sua distribuzione spaziale e alla variabile utilizzata per descriverla ed è confrontata con il segnale tramite il *rapporto segnale-rumore*. Per la temperatura, il rumore è decisamente maggiore in estate con un picco in corrispondenza del termoclino, mentre d'inverno è maggiormente presente nel Mediterraneo orientale mantenendosi costante per i primi 100 m. Tuttavia il segnale rimane pressoché dominante fino ai 100 m di profondità. Relativamente alla salinità, la variabilità interna è chiaramente legata alle zone con gradiente orizzontale di salinità più forte, come il Mare di Alboràn, il Mar Egeo e a sud del Mar Ionio. Inoltre, sia per la salinità che per la velocità della corrente il rumore è sempre predominante rispetto al segnale, fatta eccezione per il Mar Adriatico e il Golf di Gabès. Infine, per la velocità della corrente, il rumore è in ottimo accordo con l'intensità stessa della corrente: zone con corrente media alta sono caratterizzate da grande rumore e viceversa. In aggiunta, un confronto tra il rumore dato dall'ensemble precedentemente definito e da un altro composto da 5 simulazioni analoghe, ma con date di inizio tra agosto e dicembre 2020, ha permesso di ricavare delle prime informazioni sul tempo di decorrelazione tra le simulazioni, trovando che questo deve essere di almeno sei mesi, contrariamente a quanto assunto in altri studi.

CONTENTS

1	Introduction	3
2	Stochastic climate theory and the definition of noise	7
2.1	Stochastic climate models	7
2.1.1	A stochastically forced model	9
2.1.2	A negative linear feedback model	10
2.1.3	Climate applications and subsequent developments . . .	12
2.2	Noise in the climate system	13
2.3	Area under study: the Mediterranean Sea	14
3	Ocean simulations and methods	18
3.1	EAS5 system	18
3.2	Rationale of the simulations	19
3.3	Methods	21
4	Results: Characterizing the noise	24
4.1	Qualitatively verifying the presence of noise	24
4.2	Depth and area dependency of the noise	27
4.3	Signal-to-noise ratio	28
4.4	Relation with the gradients of the fields	33
4.5	Preliminary analysis on the decorrelation time scale of the sim- ulations	41
5	Conclusion and further developments	44
A	Figures	47

INTRODUCTION

Climate is a complex system with very many degrees of freedom in which different physical processes act on different temporal and spatial scales, from the micro-scale's turbulent eddies to the ocean-cryosphere interaction with a time scale of decades or centuries. Moreover, all these components interact with each other due to the inherently non-linear nature of the system itself [1]. Climatic records are characterized by a continuous variance distribution encompassing all frequencies with higher variance at lower values and, until the work of Hasselmann (1976)[2], no clear explanation was given for the observed 'red' profile of the climate variance spectra.

Hasselmann proposed an alternative model of climate variability which is not based on internal instabilities or variable external forcings and whose main assumption is that the climate system may be divided into a rapidly varying component, i.e. the atmosphere, and a slowly responding one (the ocean, the cryosphere). Thus, the variability is attributed to internal random forcing applied by the short time-scale components of the system on the slow responding part. The latter behaves as an integrator of these inputs in the same manner as a large particle interacts with an ensemble of lighter particles in the Brownian motion theory. In other words, the weather supplies the slow components with energy allowing the existence of internal variability in the climate system. Moreover, he proved that without stabilising internal feedback mechanism, climate variability would grow indefinitely. Consequently, the investigation of climate variability must be shifted from looking for a positive feedback that enhances instabilities to finding a negative feedback that allows the climate response to be a stationary process, similarly to the role of friction in the Brownian motion problem.

In Hasselmann's *stochastic climate model*, as a consequence of the time-scale separation, the response of the climate system to the random forcing can be

described to the first order as a Markov process, which is a stochastic process where each state of the system depends only on the previous state. This is obtained by replacing the original deterministic system with a stochastic one, assuming the ergodicity of the system, i.e. the time average of the original system is equivalent to the ensemble average of the stochastic one, and modeling the fast variable as a white noise. Thus, it is said to be a stochastic climate model since the variables that characterize the system are not anymore deterministic, but are to be intended as stochastic processes. Indeed, observations have shown that the behaviour of a complex deterministic system is comparable to that of a stochastic process, if the evolution of the deterministic system is defined by independent factors or events. For instance, William et al. [7] - [10] showed in a series of laboratory experiments how small scale inertia-gravity waves can induce large scale regime transitions and that in a numerical model a stochastic forcing was an appropriate representation of the inertia-gravity waves.

By doing so, a great statistical reduction of the complete climate system is achieved, and consequently, computation is eased, thanks to the time separation property of the system. That is because it allows to perform statistical closure thanks to the Central Limit Theorem, i.e. "the response of a system is statistically determined by the seconds moment of the input if the latter consists of a superposition of small independent pulses of time scale short with respect to the response time of the system itself" [2]. Hence, a stochastic approach allows to adopt a different type of parameterization for the subscale processes that are not of interest during the investigation of climate variability. In fact, bulk parameterizations are the most common: they are deterministic and based on the assumption that the unresolved scales depend on the resolved one. In terms of the Brownian motion analogy, while climate variability analysis in such deterministic models would be equal to inferring the large particles trajectories using only the interactions between them and the mean pressure applied by the lighter ones, in stochastic models the paths of the large particles are deduced by the statistics of the ensemble of the small ones. Ultimately, stochastic methods for climate prediction proved to be necessary to improve the representation of long-term climate variability and reduce uncertainty and biases [4].

The intrinsic variability identified by Hasselmann is present everywhere in the climate system and at all scales, due to both the nonlinearity and the numerous degrees of freedom of climate itself. A better understanding of its nature is essential in numerical experiments when one is interested in distinguishing between the signal given by a modification of the model and the variability due to internal processes, also called *noise*. The paper by Tang et

al. *Atmospherically forced regional ocean simulations of the South China Sea: scale dependency of the signal-to-noise ratio* [6] is based on this reasoning and it investigates the ratio between the two types of variability that affects ocean models when subjected to the atmospheric forcing: a response to the external forcing, i.e. the signal, and the unprovoked variability, called noise. The authors, using an ensemble of simulations of the ocean dynamics in the South China Sea that differ only on the initial conditions taken at different times, but subjected to the identical atmospheric forcing, show that the signal-to-noise ratio is large at large scales and weakens as the scale becomes smaller. Thus, the external forcing is dominant for large scales, while the noise thrives at small scales.

The aim of the present thesis is to picture a more detailed portrait of the intrinsic variability in the Mediterranean Sea, adopting an ensemble of ocean simulations of 2021 built with the same rationale. In other words, investigating the internal variability means characterizing the uncertainty in ocean simulations and, consequently, studying ocean climate predictability. Thus, to study climate predictability we choose to understand the sensitivity of the ocean circulation to different initial conditions given the same atmospheric forcing. The different initial conditions are considered to sample the ocean internal variability due to, but not only, mesoscale eddies, which are part of the natural variability of the oceanic fluid due to internal instabilities and non-linearities.

After verifying the presence of the noise, the focus of the analysis would be on its characterization in relation with depth and area, using temperature, salinity and current velocity as diagnostic variables. The analysis is performed by representing the noise as the seasonal average of the ensemble spread, whereas the signal is taken to be the seasonal averaged variability of the ensemble mean, and by studying both the noise itself and its relation with the signal through the signal-to-noise ratio (S/N). In order to understand the physical or computational reason behind the presence of the noise, its relation with the gradients of the corresponding diagnostic variable is investigated. Finally, a preliminary analysis of the dependence of the noise on the initial conditions of the simulations is carried out in order to provide some information for the estimate of the characteristic time of the chaotic dynamics of the system, i.e. the decorrelation time of the simulations.

Studying the presence and the role of the noise is fundamental to understand the process at play in the ocean and quantify the importance of the internal processes of the ocean itself compared to every eventual external forcing, first of all the atmospheric one. Thus, it would allow for a better comprehension of the activity of the Mediterranean Sea, which is a peculiar and highly di-

versified basin. Finally yet importantly, it aims at identifying the sources of uncertainty in ocean simulations and improving the representation of these processes in ocean models, in order to produce more accurate predictions, even as regards long-term evolution.

The present work is divided as follows: in Chapter 2 the theoretical background of stochastic climate models is given with a greater level of detail, along with a more complete definition of the noise itself. Moreover, an overview of the Mediterranean Sea and its main features is presented. In Chapter 3, the model adopted for the simulations and the rationale of the experiment are described and the methods used in the analysis are explained. Results are showed and discussed in Chapter 4 and conclusions are summarized in Chapter 5.

STOCHASTIC CLIMATE THEORY AND THE DEFINITION OF NOISE

In the present sections, the theory of stochastic climate models is introduced following Hasselmann's original formulation. Subsequently, an overview on the concept of noise or internal variability is reported and the definition adopted in this work is provided. Finally, an essential description of the Mediterranean Sea is given.

2.1 Stochastic climate models

Stochastic climate theory was conceived by Hasselmann in 1976 in his seminal paper *Stochastic climate models* [2] where he designed a reduced model based on the concept of scale separation in space and/or time.

Let $\mathbf{z} = (z_1, \dots, z_l)$ be the finite set of variables that describe the instantaneous state of the complete climate system, such as the temperature field, and let the evolution of the system be described by the following equations:

$$\frac{dz_i}{dt} = w_i(\mathbf{z}), \quad \forall i \quad (2.1)$$

where w_i are non-linear functions of \mathbf{z} .

The model assumes that the system can be divided into 2 parts $\mathbf{z} = (\mathbf{x}, \mathbf{y}) = (x_1, \dots, x_m, y_1, \dots, y_n)$ characterized by different response times $\tau_x \ll \tau_y$. Therefore, \mathbf{x} is the fast varying component, i.e. the so called weather, whereas \mathbf{y} is the slowly responding part of the climate, such as the ocean and the cryosphere. Since the time scale of the weather is of the order of a few days, while the response scale of the \mathbf{y} variable is of the order of at least several months or

years, the previous assumptions generally hold. The prognostic equations are then:

$$\frac{dx_i}{dt} = u_i(\mathbf{x}, \mathbf{y}), \quad \forall i \quad (2.2)$$

$$\frac{dy_i}{dt} = v_i(\mathbf{x}, \mathbf{y}), \quad \forall i \quad (2.3)$$

This approach corresponds to the classical statistical treatment of the Brownian motion problem, where the \mathbf{x} and \mathbf{y} can be interpreted as the position and momentum coordinates of small and large particles, respectively. However, such scale separation is common to other types of climate models, both General Circulation Models (GCM) and Statistical Dynamical Models (SDM). The difference from these deterministic models resides in the adopted time-scale and in the type of closure hypothesis: the former integrate the system using a time-scale $t \ll \tau_y$ and they are interested in following the evolution of the "weather" keeping constant all the other climatological variables, whereas the latter look at the changes of the slow components and assume that the statistics of \mathbf{x} depends on \mathbf{y} . In a stochastic model, instead, the prognostic equations are for the slow variables only and their evolution is determined also by the statistics of the fast components, which is evaluated by real data or GCMs.

For a time t in the range $\tau_x \ll t \ll \tau_y$, it is possible to define the variations of the slow variable as $\delta\mathbf{y} = \langle \delta\mathbf{y} \rangle + \mathbf{y}'$, where $\langle \delta\mathbf{y} \rangle$ is the mean component, averaged over all \mathbf{x} values for a fixed \mathbf{y} , and \mathbf{y}' is the fluctuating part, defined by the statistics of \mathbf{x} . In order to expand the validity of the previous expression to time-scales greater than τ_y , it is necessary to consider the corresponding *stochastic differential equation* (SDE):

$$\frac{dy_i}{dt} = \langle v_i \rangle + v'_i, \quad \forall i \quad (2.4)$$

with $\langle v'_i \rangle = 0$ and $\langle \delta y_i \rangle = \langle v_i \rangle t$.

Equation 2.4 is said to be stochastic since at least one of its terms is a *stochastic process* and its solution is also a stochastic process, which is a mathematical object that consists in a collection of random variables indexed by a variable t , in this case time. Examples of stochastic processes are the random walk or the Brownian motion, which will be treated in detail later. Hence, the fast variable x_i , and consequently the fluctuating component v'_i dependent on it, is taken to be a *white noise* $\xi(t)$. The latter is a random Gaussian process with zero mean, finite variance and no memory, i.e. $\langle \xi(\tau + t)\xi(t) \rangle = \delta(\tau)$. Furthermore, a white noise has the property of having a flat spectral density, i.e. $f(\omega) = \frac{1}{2\pi} \int_{-\infty}^{\infty} d\tau e^{-i\omega t} \langle \xi(\tau + t)\xi(t) \rangle = \frac{1}{2\pi} \int_{-\infty}^{\infty} d\tau e^{-i\omega\tau} \delta(\tau) = \frac{1}{2\pi}$

for every ω . Its integral with respect to time $W_t = \int_0^t ds \xi(s)$ is also a Gaussian process thanks to the Central Limit Theorem and it is called *Wiener process*. A *Wiener process* W_t is a stochastic process with the following properties: $W_0 = 0$ almost surely, its increments are independent and normally distributed, it has zero mean and variance $\sigma^2 = t$. Obviously, the time derivative of a Wiener process is a white noise. However, this type of arguments is not to be considered mathematically formal, but as an intuitive reasoning since $dW = \xi dt \simeq \sqrt{dt}$ is not a true differential. For a more precise dissertation, the reader is referred to the works of Wiener, Itô and Stratonovich [11].

2.1.1 A stochastically forced model

By considering only the equations for the fluctuating part:

$$\frac{dy'_i}{dt} = v'_i, \quad \forall i \quad (2.5)$$

one obtains a stochastic differential equation for the evolution of a Wiener process, which is the limit of a one-dimensional random walk when the step size tends to zero or, equivalently, a one-dimensional diffusion process [12]. For this reason, it is known that the variance of the fluctuating part is linearly increasing in time, i.e. $\langle y'^2 \rangle = 2Dt$ where D is the diffusion coefficient. Moreover, it is possible to derive the spectrum $G(\omega)$ of the response \mathbf{y}' by expanding the terms of equation 2.5 in the Fourier domain:

$$v'_i(t) = \int_{-\infty}^{\infty} V_{i(\omega)} e^{i\omega t} d\omega$$

Its Fourier components are statistically orthogonal, being it a stationary process:

$$\langle V_i(\omega) V_{*j}(\omega') \rangle = \delta(\omega - \omega') F_{ij}(\omega)$$

with $F_{ij}(\omega) = \frac{1}{2\pi} \int_{-\infty}^{\infty} \langle v'_i(t+\tau) v'_j(t) \rangle e^{-i\omega\tau} d\tau$ being the cross-spectrum of the input $v'_i(t)$, i.e. the Fourier transform of the cross-covariance. Since $\langle v'_i(t+\tau) v'_j(t) \rangle = \delta_{ij} \delta(\tau)$, $F_{ij}(\omega)$ is constant too. Consequently, by integrating in t , it is found for the response $y'_i(t)$:

$$y'_i(t) = \int_{-\infty}^{\infty} Y_{i(\omega)} e^{i\omega t} d\omega - \int_{-\infty}^{\infty} Y_{i(\omega)} d\omega$$

where $Y_i(\omega) = \frac{V_i(\omega)}{i\omega}$. Analogously, the cross spectrum $G_{ij}(\omega)$ for $y'_i(t)$ is found easily as:

$$G_{ij}(\omega) = \frac{F_{ij}(\omega)}{\omega^2} \quad (2.6)$$

Thus, by considering only the presence of fluctuations, the cross-covariance of the response in the range $\tau_x \ll t \ll \tau_y$ grows linearly in time. Similarly, the cross spectrum of the response decreases with ω^2 with a singularity in $\omega = 0$, meaning that the changes of the slow variable happen at low frequencies, as expected from the white spectrum of the input for frequencies in the range $\frac{1}{\tau_y} \ll \omega \ll \frac{1}{\tau_x}$.

It is clear that such dissertation can be repeated with an input different from a pure white noise, but that tends to it for $\omega \ll \frac{1}{\tau_x}$, that is it has a zero covariance and constant spectral density in that time range. For instance, an *Ornstein-Uhlenbeck process* [13] can be chosen, that is a stationary stochastic Gaussian-Markov process, defined by the following stochastic differential equation:

$$dx_i = -\gamma x_i dt + \sigma dW_t^i \quad (2.7)$$

where $\gamma = \frac{1}{\tau_x} \gg 1$ and $\sigma > 0$ and dW_t denotes a Wiener process. By exploiting Itô calculus, it can be proven that the solution is $x_i(t) = \int_0^t e^{-\gamma(t-s)} dW_s^i$ and it has the following properties:

$$\langle x_i(t) \rangle = 0 \quad (2.8)$$

$$\langle x_i(t)x_j(t+\tau) \rangle = \langle x_i(t)x_j(s) \rangle = \delta_{ij} \frac{e^{-\gamma|t-s|} - e^{-\gamma(t+s)}}{2\gamma} \xrightarrow{t \rightarrow \infty} \frac{e^{-\gamma\tau}}{2\gamma} \quad (2.9)$$

$$\langle x_i(t)^2 \rangle = \frac{1 - e^{-2\gamma t}}{2\gamma} \xrightarrow{t \rightarrow \infty} \frac{1}{2\gamma} \quad (2.10)$$

After a sufficient time $t \gg \tau_x$, the covariance is independent of time t and if $\tau\gamma \gg 1$ it tends to a δ -function $\delta(\tau)$.

Note that the two different assumptions on the type of stochastic forcing correspond to the two different stochastic calculi: Itô and Stratonovich. The former has uncorrelated noise forcing while the latter assumes a finite correlation between noise increments.

In conclusion, in order to obtain a realistic climate model for $t \gg \tau_y$, some feedbacks need to be included, i.e. equation 2.4 is to be considered. Moreover, since \mathbf{y} is a random variable, the evolution equation should be written for its probability density distribution $p(\mathbf{y}, t)$.

2.1.2 A negative linear feedback model

First, it is assumed that \mathbf{y} is a *Markov process*, that is a stochastic process such that the conditional probability $P(y_1, \dots, y_{n-1}|y_n)$ that \mathbf{y} lies in the interval $(\mathbf{y}_n, \mathbf{y}_n + d\mathbf{y}_n)$ at time t_n depends, apart from \mathbf{y}_n , only on the value of \mathbf{y} at the

previous time t_{n-1} . Consequently, a Markov process is completely determined by the firsts two moments of the distribution of Δy :

$$A(y) = \lim_{\Delta t \rightarrow 0} \frac{\langle \Delta y \rangle}{\Delta t}, B(y) = \lim_{\Delta t \rightarrow 0} \frac{\langle \Delta y^2 \rangle}{\Delta t} \quad (2.11)$$

From the Markovianity of the process, it is possible to deduce the *Smoluchowski equation*, which is the essential ingredient for the theory:

$$P(\mathbf{x}|\mathbf{y}, t + \Delta t) = \int d\mathbf{z} P(\mathbf{x}|\mathbf{z}, t) P(\mathbf{z}|\mathbf{y}, \Delta t) \quad (2.12)$$

From the integral $\int_{-\infty}^{\infty} d\mathbf{y} R(\mathbf{y}) \frac{\partial P(\mathbf{x}|\mathbf{y}, t)}{\partial t}$, where $R(\mathbf{y})$ is an arbitrary function that goes to zero for $y \rightarrow \pm\infty$, and exploiting relation 2.12, the *Fokker-Planck equation* for a generic Markov process is derived [3]:

$$\frac{\partial P}{\partial t} = - \sum_i \frac{\partial}{\partial y_i} [A_i(\mathbf{y}) P] + \frac{1}{2} \sum_{k,l} \frac{\partial^2}{\partial y_k \partial y_l} [B_{k,l}(\mathbf{y}) P] \quad (2.13)$$

where A_i and $B_{k,l} = \langle y'_i y'_k \rangle = 2D_{k,l}$ are the first and second moments as defined before.

This equation returns the evolution of the probability distribution of a Markovian system starting from an arbitrary distribution and it is characterised by a propagation and a diffusion part, with the corresponding coefficients A and B , respectively. Furthermore, it is the diffusion component that is responsible for the stochasticity of the system and the spreading of the probability distribution at later times.

It is important to notice that the Fokker-Planck equation and the corresponding SDE describes the evolution of the same system under a different light.

A solution to the FPE can be found invoking the Central Limit Theorem for $D_{ij} = D$ constant and for $\langle v_i \rangle = -\beta_i y_i$ with $\beta_i > 0$ for all i , which gives:

$$\frac{dy_i}{dt} = -\beta_i y_i + v'_i, \quad \forall i \quad (2.14)$$

which is the *Langevin equation* for the *Brownian motion* problem of a free particle. Note that equation 2.14 and equation 2.7 are equivalent, meaning that \mathbf{y} is an Ornstein-Uhlenbeck process.

The Brownian motion represents the apparently random movement of particles in a medium subjected to collisions with the molecules of the fluid. The Langevin equation, that is a SDE, represents the time evolution of the velocity of the particle under the effect of the viscous force (*dissipation*) and of collisions (*fluctuations*). In this case, $A_i = -\beta_i y_i$ and $B_{ij} = 2D$ and the solution is:

$$p(\mathbf{y}, t) = \frac{1}{\sqrt{(2\pi)^n \det(R)}} \exp \left[- \frac{(y_i - \bar{y}_i)(y_j - \bar{y}_j)}{2R_{ij}} \right] \quad (2.15)$$

where $\bar{y}_i = y_{i0}e^{-\beta t}$ is the mean and $R_{ij} = [(y_i - \bar{y}_i)(y_j - \bar{y}_j)] = \frac{2D_{ij}}{\beta_i + \beta_j}(1 - e^{-(\beta_i + \beta_j)t})$ is the covariance tensor.

As regards the cross-spectrum $G_{ij}(\omega)$ of the response, it can be easily deduced by substituting the Fourier expansion of both v'_i and y_i in 2.14 and assuming to deal with a stationary process, i.e. to be at $t \gg \tau_x$:

$$G_{ij}(\omega) = \frac{F_{ij}(\omega)}{(\omega - i\beta_i)(\omega + i\beta_j)} \quad (2.16)$$

Therefore, in the case of negative linear feedback the response tends to a stationary distribution at large t . Coherently, the cross-spectrum of the response resolves its singularity and has a finite peak at $\omega = 0$, modulated by the eigenvalues of the feedback matrix. However, in the time range $\tau_x \ll t \ll \tau_y$ the behaviour is the same as in the case of pure fluctuations.

In conclusion, thanks to the two-timing property of the climate system, the response of the slow component forced by the fast variables can be modeled as a continuous random walk or diffusion process. However, in order to obtain physical results and avoid an indefinite growth of climate variability, negative linear feedbacks need to be introduced. The evolution of the resulting system follows the same stochastic differential equation as a free particle in Brownian motion theory, i.e. it is a Ornstein-Uhlenbeck process.

2.1.3 Climate applications and subsequent developments

The canonical example of the application of the rationale of stochastic climate models was given by Frankignoul and Hasselmann [14]. They showed that sea surface temperature (SST) anomaly can be explained at a first-order by an elementary mixed layer model where the atmosphere introduces a white-noise forcing and the ocean acts as a Markov integrator of the stochastic input. This led to the first types of stochastic models, i.e. Linear Inverse Models, which use a linearized dynamics and introduce an additive white noise and a friction term, in order to obtain only stable solutions. However, this approach can be adopted only to a process with Gaussian statistics, limiting its range of applications. It has been proven, especially in the study of extreme events, that the choice of a multiplicative noise allows for the emergence of non-Gaussian statistics [4]. Moreover, all of these reasoning is based on the assumption of a memoryless (Markovian) process due the two-timing property of the climate system, which is true only as a first approximation since the climate spectrum has no clear truncation. Consequently, memory effects need to be introduced, which lead to non-Markovian processes. In fact, these are the reasons behind the subsequent developments of stochastic climate models.

Numerous studies have proven how stochastic models allow to successfully reproduce physical phenomena in a more computationally efficient way, e.g. from the spectra of the Quasi-Biennial Oscillation (QBO) and of El Niño Southern Oscillation (ENSO) it was shown how these modes of climate variability are excited by fast-scales fluctuations. Moreover, it has been displayed that an Ornstein-Uhlenbeck spectrum is reproduced only in the superficial layer of the ocean, whereas at greater depth ocean stratification shields lower levels from surface fluctuations, leading to a different type of variability (von Storch et al.[1]). According to Palmer [5], stochasticity must be adopted for every climate model, regardless of how comprehensive it is, since it leads to "more accuracy with less precision", by reducing the degrees of freedom of the system through statistical closure. Furthermore, he argues that deterministic parametrization is suitable only when a clear scale separation between the resolved and the unresolved scales is present, which is not the case in reality where multiscale situations are much more frequent.

In conclusion, stochastic parameterizations have been shown to provide more skillful forecasts than traditional ensemble prediction methods. For further details on following developments of statistical approach to stochastic models, which are beyond the scope of this thesis, please refer to Franzke et al. [4] and Palmer [5].

Since the rationale behind stochastic climate models has been established, in the following section an overview of the concept of "noise" in climate physics is performed and the definition adopted in the present study is given.

2.2 Noise in the climate system

From the definition reported in the Glossary of Meteorology of the American Meteorological Society, the so called *climate noise* comprehends all the "variations in the state of the climate system that have little or no organized structure in time and/or space". However, it is important to notice that it is a relative term, since some variations can be considered noise in a certain context and not in another. In other words, every process that develops at time-scales or spatial scales smaller than those analyzed can be treated as a noise with respect to the signal under study. It is clear that the concepts of signal and noise can be applied in different contexts, for instance when investigating the role of the anthropogenic forcing in climate change as compared to natural variability [15]-[17]. The aim is to filter the signal from the noise that is masking it. Consequently, as a diagnostic tool, the signal-to-noise ratio is often considered. In other words, it is in these *detection* problems, i.e. being able to tell if by adding a modification to the model the resulting differences

are due to it and not to internal variations that would have been present in any case, that the noise needs to be considered. Indeed, the meaning of the presence of noise is that the effect of a modification in a numerical experiment may no longer be simply described as the plain difference between a modified simulation and a control simulation [6].

As already said and proven, in stochastic climate theory these subgrid processes or fast components represent a fundamental energy source for the climate system, allowing for its *internal variability*, which is the component of climate variability not due to the external forcing. Consequently, these modes of internal variability are not resolved since stochastic models focus on the accurate simulation of the large, predictable scales, while only the statistical properties of the small, unpredictable, scales are captured. Thus, this unprovoked variability could come from a plethora of phenomena such as variations in river discharge, waves or small scale eddies.

Furthermore, it is evident that for chaotic systems is extremely difficult to disentangle the model error, for instance resulting from the adopted parametrization, from the initial condition error, given by the sensitivity of the system on ICs, or from some rounding error. Consequently, the noise would generally consists in all of them, if a distinction is not possible.

In the present study, as in the paper by Tang et al. [6], the noise is to be intended as the component of the variability of the ocean that is not due to the atmospheric forcing, which is instead identified with the signal. Consequently, it is to be attributed to internal processes of the ocean itself, mesoscale eddies in the first place, so it will be called equivalently *intrinsic* or *internal ocean variability*. Nonetheless, even though it is neither of interest to study the exact sources and processes behind the formation of the noise at a certain location nor possible, a good comprehension of its properties such as time and spatial scales, depth and area distribution is sought, along with the identification of the types of processes that triggers it.

In the next section, an overview of the main features of the Mediterranean Sea is given, in order to better understand the basis of the present work.

2.3 Area under study: the Mediterranean Sea

The Mediterranean Sea (please refer to *Oceanography of the Mediterranean Sea*, [19] for a much wider dissertation) is a semienclosed basin located between 5°E and 36°W and between 32° and 46°N with average depth of 1500 m. It is connected to the Atlantic Ocean through the Strait of Gibraltar and to the Marmara Sea, and consequently the Black Sea, through the Dardanelles and the Bosphorous Strait.

CHAPTER 2. STOCHASTIC CLIMATE THEORY AND THE DEFINITION OF NOISE

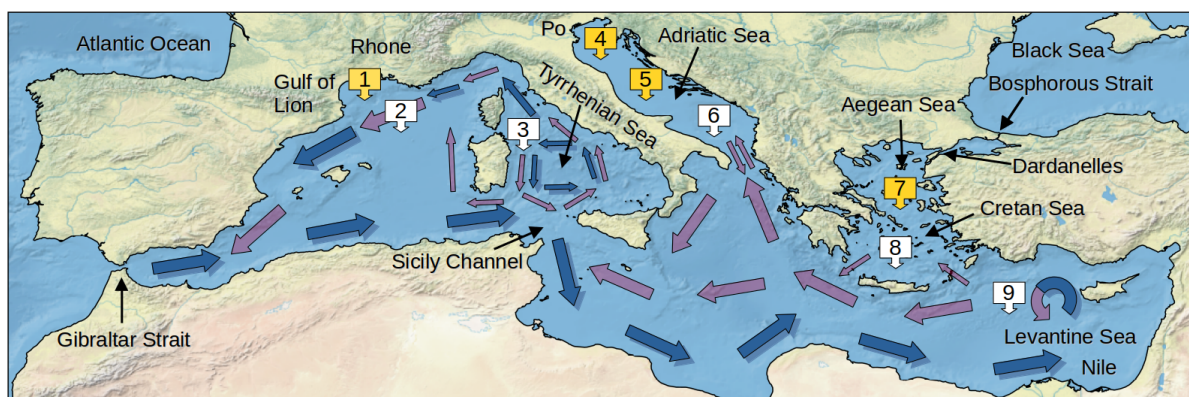


Figure 2.1: The Mediterranean Sea and its thermohaline circulation: in blue the surface flow of the AW, in purple the deep flow of the IW. The boxes indicate the regions of Deep and Intermediate Water Formation: the white ones indicate open ocean convection areas, while the yellow ones shelf dense water cascading areas.

The circulation in the Mediterranean basin is determined by its freshwater deficit ($E - P > 0$), i.e. the evaporation is greater than the freshwater input given by river runoff and precipitation. Thus, a two-way flow at the Strait of Gibraltar is necessary to allow for the conservation of water and salinity: an inflow at the surface from the Atlantic Ocean into the Mediterranean Sea and an outflow at depth in the opposite direction compensate for freshwater losses and act to conserve the salinity balance. In fact, the predominance of evaporation in the Mediterranean basin causes its seawater (MW) to be saltier, hence denser, than Atlantic waters (AW) and, consequently, the outflow is situated below the inflow. This type of circulation is called *antiestuarine*, since it behaves as an inverse estuary.

At the surface, the wind stress is responsible for the permanent gyres of the basin, whereas the heat and freshwater fluxes determine the thermohaline circulation and the consequent deep water formation processes.

As regards the wind stress, the strongest winds are situated in the Levantine Basin in summer and in the Gulf of Lion in winter.

The annual net heat flux implies a small loss of -4 W/m^2 , in order to match the heat gain through the Strait of Gibraltar from the Atlantic Ocean. Moreover, the annual heat budget is characterized by an overall loss in the northern part of the basin (-30 W/m^2) and a gain in the southern part (50 W/m^2), even though strong seasonal variations are present: in summer the entire basin gains heat, while in winter it experiences heat loss particularly strong in the Aegean Sea. Overall, the heat balance is ruled mostly by the shortwave term,

particularly influent as latitude decreases, and the latent heat loss, which is instead stronger in the regions with intense wind forcing.

Finally, the freshwater balance is always in deficit, apart from the Adriatic Sea and some coastal regions where the net evaporation is compensated by precipitation.

The Mediterranean thermohaline circulation (Figure 2.1), which is overall cyclonic, is formed by three main water masses: the *Atlantic Water* (AW), which flows in the mixed layer and in the thermocline, the *Intermediate Water* (IW) and the *Deep Water* (DW), that instead are located below the thermocline. The former is the lightest and less salty water mass, it enters through the Strait of Gibraltar, follows the North-African coast and splits into two branches in the Sardinia Channel, one that flows counterclockwise in the Tyrrhenian Sea and then follows the northern boundaries of the Western Mediterranean (WMed), and the other that crosses the Sicily Channel and enters the Eastern Mediterranean (EMed). During its permanence in the Mediterranean basin, the AW is modified and becomes colder (due to cold and strong winds) and less salty in the WMed and warmer and saltier in the EMed, where the evaporation is more intense, implying a net distinction between the two areas of the Med Sea. The salinity field has instead a minimum in correspondence with the main regions of freshwater inputs: the Strait of Gibraltar, the Dardanelles and the deltas of the main rivers such as the Po, the Nile and the Rhone.

The IW forms in the Levantine and Cretan Sea, due to the high evaporation rate of these regions, and it is found at the depths of 250-600 m. Once it is formed, it travels towards the WMed crossing both the Adriatic, the Tyrrhenian Sea and the northern WMed, helping in the formation of DWs in these regions, and finally crosses the Strait of Gibraltar, forming the main part of the outflow.

Deep Water forms at different locations (boxes in Figure 2.1) in the northern part of the basin (Aegean Sea, Adriatic Sea, Gulf of Lion) due to the presence of strong, cold and dry winds such as the Bora and the Mistral, during winter-early spring. Deep Water Formation happens following two processes, both present in the Mediterranean: *dense shelf water cascading* and *open ocean convection*. In both cases, strong and cold winds causes evaporation and cooling of the surface layers, producing denser water at the surface that eventually sinks. In the case of shelf water, it *cascades* out of the shelf, forming deep or intermediate waters, and could contribute to the process of open ocean convection. The latter takes place in the open sea following three steps: first, at the horizontal scales of a cyclonic gyre (100 km), an area of dense water is created, followed by violent mixing along the vertical column at the scales of *plumes* (1 km). Once the patch of dense water is formed, it spreads

away from the convection area thanks to eddies (10 km) and stratification is re-established with the new dense water patch located at the bottom. DW forms a significant component of the water column, but maintains itself nearly constant, as regards temperature and salinity, at all depth levels. Moreover, due to the presence of bathymetry, the two deep water masses of the WMed (WMDW) and of the EMed (EMDW) remain separate, the latter being warmer and saltier than the former.

In the next chapter, the rationale of the experiment and the adopted methods are presented.

OCEAN SIMULATIONS AND METHODS

In this chapter, in order to introduce the analysis and to understand the results, the technical features of the study are presented.

First, an overview of the model adopted for the analysis is reported, then an explanation of the scheme of the performed simulations is given along with a presentation of the type of analysis that is carried out.

3.1 EAS5 system

The model used in this study is the EAS5 system [18], a coupled hydrodynamic-wave model implemented over the whole Mediterranean Basin and the adjacent area of the Atlantic Ocean (Figure 3.1) and developed by the CMCC. It is the precursor of the current operational modeling system adopted by the Copernicus Marine Service (EAS6 system) that was introduced in 2021 and whose main difference from the EAS5 system is the presence of tides.

The model horizontal grid resolution is $1/24^\circ$ (ca. 4 km) and has 141 unevenly spaced vertical levels. The hydrodynamics is supplied by the Nucleus for European Modelling of the Ocean (NEMO v3.6) while the wave component is provided by Wave Watch-III. NEMO model is discretized on a staggered grid (Arakawa C grid) with masking of land areas. The model is forced by momentum, water and heat fluxes computed by bulk formulae using the $1/10^\circ$ horizontal-resolution operational analysis and forecast fields from the European Centre for Medium-Range Weather Forecasts (ECMWF). The Mediterranean modeling system is forced in the Atlantic side by the Global analysis and forecast product, while in the Dardanelles Strait it is forced by a combination of daily climatological fields from a Marmara Sea model and the Global analysis and forecast product. The water balance is computed as Evaporation

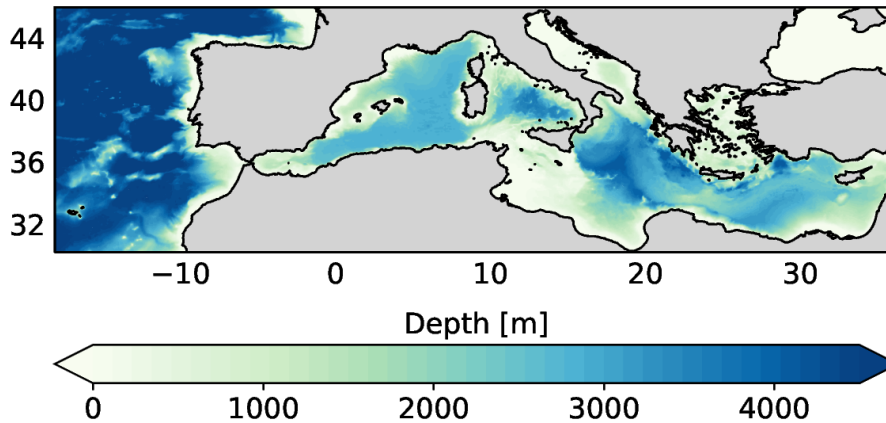


Figure 3.1: Numerical domain of the EAS5 system and its bathymetry.

minus Precipitation and Runoff. The evaporation is derived from the latent heat flux, precipitation is provided by ECMWF, while the runoff of the 39 rivers implemented is provided by monthly mean datasets except for the Po river runoff which is provided as daily mean observations.

The 10-days daily forecast fields are produced every day.

The available variables are, for instance, temperature, salinity, horizontal and vertical velocity, sea surface height, mixed layer depth.

3.2 Rationale of the simulations

Following the idea in Tang et al. (2019) [6], an ensemble of ten simulations of the Mediterranean Sea is generated with the same atmospheric forcing, but with different start dates and consequently different run times (Table 3.1). The analyzed year is 2021, which is the only year covered by all the simulations (Figure 3.2). Furthermore, for the purposes of the analysis, the ensemble is halved by distinguishing between the so called *multi-year ensemble* (red) and the *single-year ensemble* (blue), which are formed by the simulations initiated one year after the other and by those that started all in 2020 separated only by a month, respectively. By building the ensemble in this way, it is possible to generate noise without perturbing the system with *ad hoc* perturbations. Indeed, since the initial conditions of the simulations are taken from the available reanalyses, the difference among the simulations are caused by the data assimilation scheme. In fact, the initial condition of a simulation with a later start date does not coincide with the outcome of a previous simulation, but it is the result of the analysis step of the data assimilation scheme, where the simulation is compared with real data and readjusted. It is clear that the

further back is the start date of the simulation, the longer has passed from the last analysis.

The diagnostic variables used in the present work are primarily temperature (°C), salinity (10^3 ppm) and horizontal velocity (m/s).

	Start time	End time	Total run time
S1	01/01/2016	31/12/2021	72 months
S2	01/01/2017	31/12/2021	60 months
S3	01/01/2018	31/12/2021	48 months
S4	01/01/2019	31/12/2021	36 months
S5	01/01/2020	31/12/2021	24 months
S6	24/08/2020	31/12/2021	about 16 months
S7	28/09/2020	31/12/2021	about 15 months
S8	26/10/2020	31/12/2021	about 14 months
S9	23/11/2020	31/12/2021	about 13 months
S10	28/12/2020	31/12/2021	about 12 months

Table 3.1: Start dates for each of the 10 simulations: in red the multi-year ensemble members, in blue the single-year ensemble members.

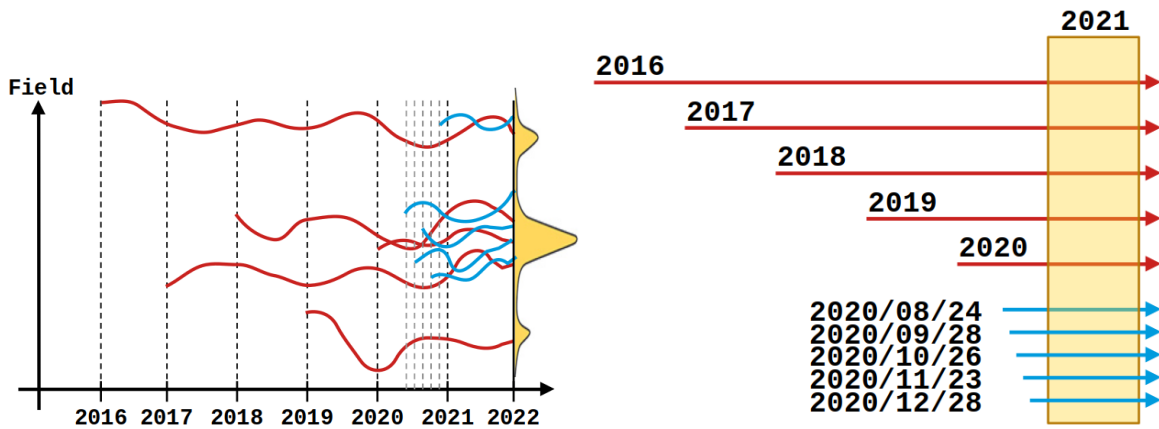


Figure 3.2: Schemes of the rationale of the simulations: in red the members of the multi-year shifted ensemble, in blue those of the single-year shifted ensemble and the yellow box represents the year of study, i.e. 2021.

3.3 Methods

First, to verify the presence of differences among the simulations, i.e. noise, the logarithm of the barotropic velocity is computed for each simulation, as in the work by Tang et al. [6]. Since the depth levels are unevenly spaced, the mean along the vertical direction is calculated as a weighted average with the weights equal to the ratio of the thickness d_k of each layer k over the maximum depth $D_{i,j}^{max}$ at each grid point (i, j) . The barotropic speed is then:

$$v_{i,j}^{bar} = \sqrt{(u_{i,j}^{bar})^2 + (v_{i,j}^{bar})^2} = \sqrt{\left[\sum_{k=1}^{k_{i,j}^{max}} u(i, j, k) \frac{d_k}{D_{i,j}^{max}} \right]^2 + \left[\sum_{k=1}^{k_{i,j}^{max}} v(i, j, k) \frac{d_k}{D_{i,j}^{max}} \right]^2} \quad (3.1)$$

Then, to obtain a more detailed representation, the time series of the selected variables are considered. The locations for these time series are chosen in order to give a good coverage of the Mediterranean basin and, simultaneously, to analyze the areas of deep/intermediate water formation [19], in order to give a complete picture of the depth dependency of the noise. Figure 3.3 and Table 3.2 show the exact locations of these points and their maximum depth, along with the names with whom they will be addressed in the present thesis.

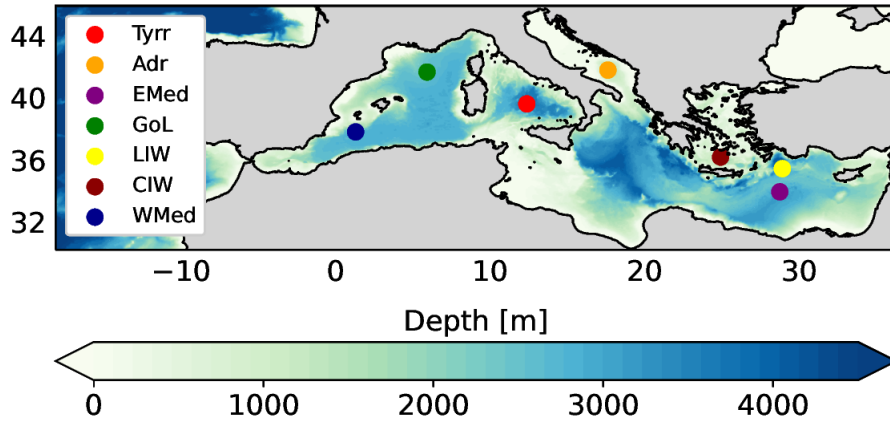


Figure 3.3: Bathymetry of the Mediterranean Sea with the dots that indicate the locations chosen for the analysis.

Subsequently, a scale separation of the time series is performed to characterize the time-scale of the differences among the simulations for each field. The low frequency component of the field is obtained through a running mean over

Location	Entire name	Depth
Tyrr	Tyrrhenian Sea	3500 m
Adr	Adriatic Sea	1095 m
EMed	Eastern Mediterranean Sea	2880 m
GoL	Gulf of Lion	2530 m
LIW	Levantine Intermediate Water	3100 m
CIW	Cretan Intermediate Water	920 m
WMed	Western Mediterranean Sea	2665 m

Table 3.2: Locations chosen for the analysis of the time series.

a period T of 30 days, which essentially corresponds to a 30 days low-pass filter, whereas the fast varying part is computed by subtracting the averaged one from the complete field f :

$$f(t_j) = f_{low}(t_j) + f_{high}(t_j) = \frac{1}{T} \sum_{i=-T/2}^{T/2} f(t_{j+i}) + f_{high}(t_j) \quad (3.2)$$

The choice of a 30 days period is due to the fact that it seems an appropriate time window to filter out fast disturbances and characterize the average trend over the entire year. Note that, to avoid considering all 141 vertical levels, often only 7 of them are reported, corresponding to the depths of 1 m, 20 m, 50 m, 100 m, 200 m, 500 m and 1000 m.

For the subsequent analysis, only the multi-year ensemble is considered, since the two ensembles are not equivalent (see Section 4.2).

Thus, adopting the multi-year simulations, the *ensemble spread* relative to the field f , which is intended to be a representation of the noise, defined as:

$$\sigma(i, j, t) = \frac{1}{N_e} \sqrt{\sum_{s=1}^{N_e} [f_s(i, j, t) - f_{ave}(i, j, t)]^2} \quad (3.3)$$

is investigated, where f_s is the chosen field as given by the s -th simulation and f_{ave} is the ensemble mean. Its values over the entire basin during two different seasons, January-February-March (**JFM**) and July-August-September (**JAS**), is computed for the depth levels previously indicated. Furthermore, its vertical profile, as a time average of the months of August and February, at the 7 chosen locations is considered.

Lastly, the *signal-to-noise ratio* is computed as the ratio of the standard deviation of the ensemble mean f_{ave} over the season and the average ensemble spread σ over the same period:

$$\mathbf{S/N}(i, j) = \frac{std(f_{ave})_t}{mean(\sigma)_t} = \frac{\sqrt{\sum_{t_{in}}^{t_{fin}} [f_{ave}(i, j, t) - \bar{f}_{ave}(i, j)]^2}}{\sum_{t_{in}}^{t_{fin}} \sigma(i, j, t)} \quad (3.4)$$

Thus, it gives information about the importance of the ensemble spread (noise) with respect to the corresponding temporal variations of the ensemble mean (signal). Larger values of this ratio corresponds to predominance of the signal, i.e. the atmospheric forcing is the dominant factor at play in the variations of the ocean, whereas a S/N less than unity implies a thriving noise, i.e. some other processes both of physical and computational origin determine the variability.

In addition, a preliminary analysis on the characteristic time scale of the chaotic dynamics, i.e. the time necessary to pass to decorrelate the simulations so that their differences are only due to the chaotic nature of the system itself and not to its dependence on initial conditions, is carried out by comparing the two ensembles through the difference between their spreads. By comparing the single-year and the multi-year ensemble spreads one could check if the time passed for the latter from initialization to analyzing the data is enough so that the initial state is not of importance anymore. If it holds, no systematic differences should be present between the two ensemble spreads, since they would be statistically equivalent. On the other hand, if a noticeable difference is found it means that some information about the characteristic time scale can be deduced, for instance if the assumption of one month adopted in Tang et al. [6] is correct or not. In other words, by studying the noise predicted by two different ensembles of simulations of the same system, subjected to the same forcing, an estimate of the sensitivity of the system on initial conditions can be performed. Indeed, this is useful, and needs to be studied in detail, in the analysis of internal variability since it would allow to understand what is the correct time scale to consider in order to have uncorrelated simulations.

RESULTS: CHARACTERIZING THE NOISE

In this section, the results for the analysis of the noise in the Mediterranean Sea are presented. Note that, in the present dissertation, the terms *ensemble spread* and *noise* would be used indiscriminately, since the former is the chosen numerical representation of the latter. The majority of the plots relative to this chapter are reported in Appendix A: Figures.

4.1 Qualitatively verifying the presence of noise

First, the presence of differences among the simulations is verified by intuitively studying the fields obtained from each of them.

In Figure 4.1, the field of the natural logarithm of the barotropic velocity, on the 01/08/2021, is plotted as obtained from each simulation of the multi-year ensemble. It is clear that, even though the main features and orders of magnitude of the circulation are reproduced in a very similar way among the simulations, such as the stronger currents in the Sicily Channel and the milder ones in the central part of the basin, the five simulations differ for the representation of smaller scales structures, such as eddies. Moreover, a better match among them is found for the strength of the circulation than for the direction of the streamlines. These distinctions suggest that the noise is mostly present at smaller scales, whereas the shared large-scale features are to be attributed to some external forcing, such as, but not only, the atmospheric one (in agreement with the results by Tang et al [6]).

To further show the presence of noise among the simulations, the time series at the seven chosen locations are considered and a time-scale separation is applied using a threshold of 30 days to distinguish between high and low frequency components (see Section 3.3), in order to characterize the noise at

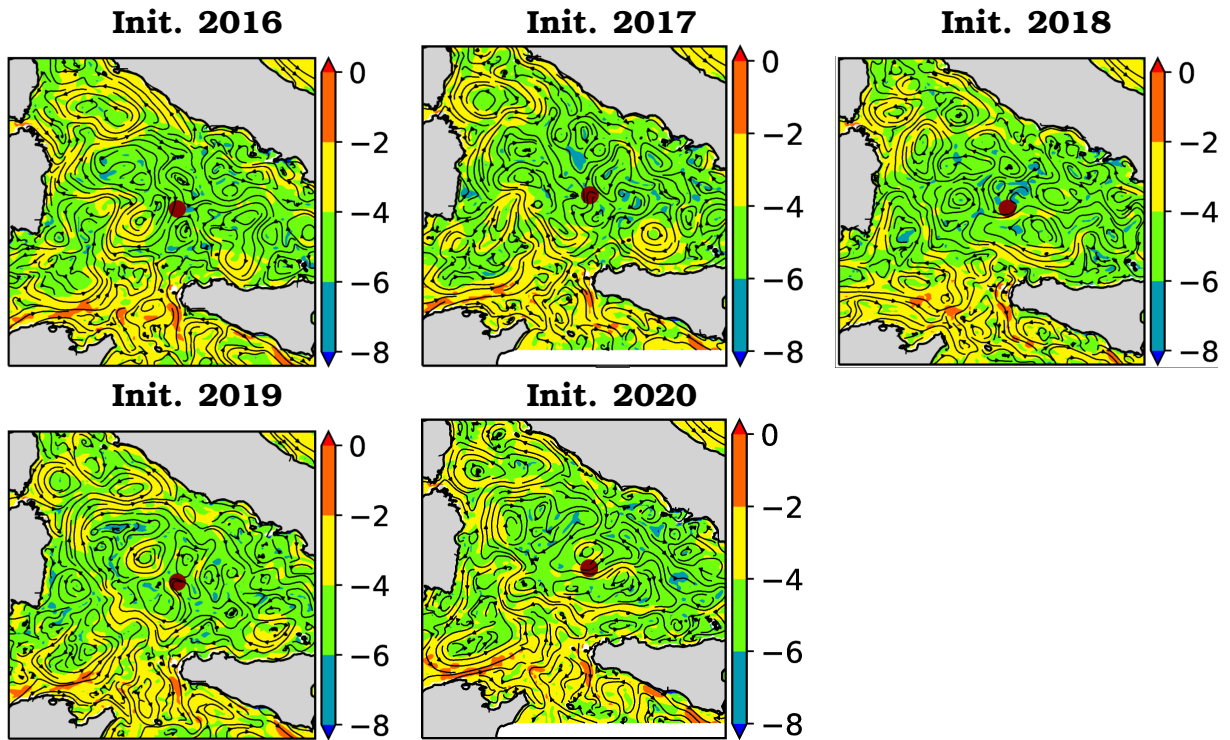


Figure 4.1: Natural logarithm of the barotropic velocity on August 1st 2021 in the Tyrrhenian Sea, as obtained from the five simulations of the multi-year ensemble. The red dot indicates the location *Tyrr*, one of those chosen for the analysis.

different time frequencies (see Figure 4.2 as an example). It can be deduced that a good agreement among the simulations is detectable for the high frequency components up to 50 m, whereas the slow components are highly correlated for the superficial layer, due to the atmospheric forcing, but significant differences start to appear already at 20 and 50 m.

By comparing the low-frequency components (the low-pass filter allows for a clearer view) of the time-series of temperature, salinity and zonal velocity at two very different locations, the Adriatic Sea (*Adr*) and the Western Mediterranean (*WMed*), it is possible to verify how this preliminary analysis reflects the distinct features of these two basins. The location in the Adriatic Sea, which is an area of Deep Water Formation (see Chapter 2), is highly dependent on the atmospheric forcing, due to the influence of the wind stress on the process. Consequently, the simulations for temperature can be superposed one to the other at the surface, reflecting a dominant role of the atmosphere, and maintain an high correlation all along the vertical direction, in particular

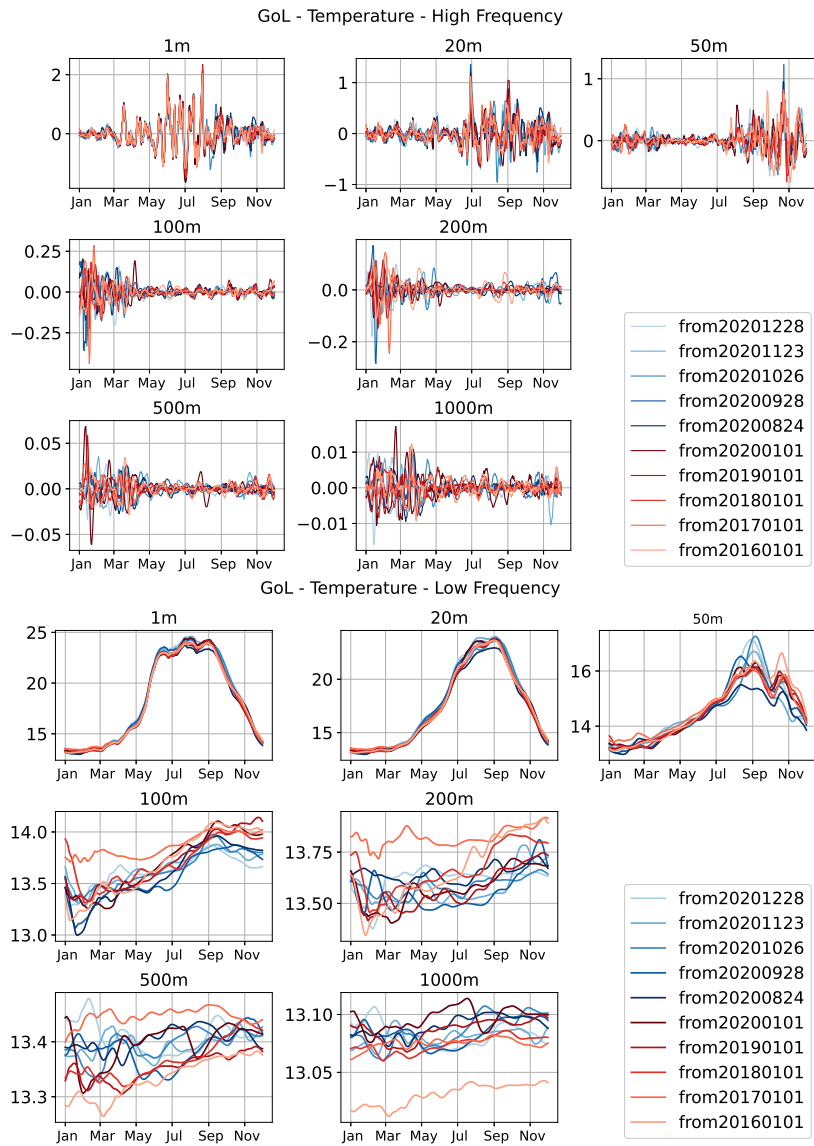


Figure 4.2: Time-scale separation of the time series of temperature in the Gulf of Lion (GoL), as given by the ten ocean simulations of 2021. High frequencies (< 30 days) on top, low frequencies on the bottom (> 30 days). In red those of the multi-year ensemble, in blue the members of the single-year ensemble.

at depth (1000 m). For salinity, the simulations show the same trend, but they have shifted values, especially at the surface. On the other hand, the Western Mediterranean is the region subjected to the water inflow and out-flow processes through the Gibraltar Strait between the Mediterranean basin and the Atlantic Ocean. Thus, it shows much more random relations among

the simulations for both scalar quantities and a much lower correlation, in particular at depth. Instead, as regards the zonal velocity, the profiles of the simulations appear to be fluctuating in an independent manner one from the other in both regions, as expected.

One important feature, shared to both location and at all depth levels, is the tendency of the single-year ensemble to show a smaller spread compared to the multi-year ensemble. For instance, the simulations for temperature at 1000 m depth in the Adriatic Sea clearly shows this. Moreover, the two ensemble are often evidently distinguishable one from the other, particularly in the case of salinity and temperature: for example, the two ensembles for the temperature simulations at the *WMed* at 50 m depth clearly diverge from each other, from July to November, leading to a sort of bifurcation.

Nevertheless, a more formal dissertation is needed, to better characterize the properties of the noise.

4.2 Depth and area dependency of the noise

The resulting maps of the ensemble spread, computed as explained in Section 3.3, are reported in the Figures A.3 - A.7 for both seasons (JAS and JFM) and for different depth levels: 1 m, 20 m, 50 m, 100 m and 500 m. Note that the following results are related only to the examined year 2021.

Overall, it is evident that the ensemble spread is seasonal: it is greater in summer for both scalar quantities (temperature and salinity) and in winter for the current velocity.

During summer, the ensemble spread for temperature (Figure A.3) has a maximum at about 20 m depth with values of the order of 0.8 - 1 °C and more around the entire basin except for the Adriatic Sea and the Gulf of Gabès, which have the smallest values of the noise at all depth levels. At the surface, instead, the highest values are found in the Balearic Sea, in the Alboràn Sea and in the Strait of Messina, while below the thermocline, at depths of at least 50 m, in the Eastern Mediterranean, especially along the coast. In winter the highest values (about 0.7 °C) are located in the Eastern Mediterranean in the first 100 m, where the vertical profile maintains itself constant.

For salinity, the areas characterized by the greatest values of the spread (0.3×10^3 ppm or more) can be easily identified and are the Aegean Sea, the region south of the Ionian Sea and the Western part of the basin from the Ebro Delta to the Gibraltar Strait. A similar pattern is found both in summer and in winter, even though the spread is greater in summer. Moreover, while in the other regions the spread tends to decrease with depth and have higher values in the first 20 m, along the coasts of Spain and Morocco and in the Alboràn Sea

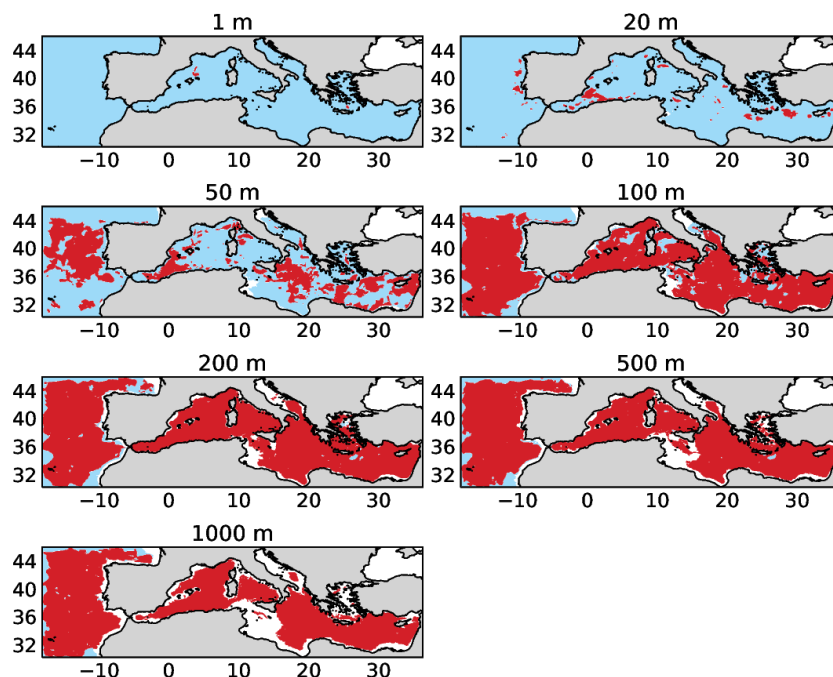
the spread has a maximum at a depth of 100 m in winter.

Finally, for current velocity, larger values of the spread (about 0.1 m/s) are visible in winter at the surface, even though its pattern is almost constant with depth while slowly decreasing its intensity, and the regions where it thrives are the Western Mediterranean, in particular the Alboran Sea and the coast of Morocco and Algeria, and in the Eastern Mediterranean along the Egyptian coast, whereas is smaller in the Adriatic Sea and in the Gulf of Gabès.

The time series of the ensemble spread (Figure A.8) of the different variables at the chosen locations and at different depth levels confirm these results.

4.3 Signal-to-noise ratio

In order to quantify the importance of the noise with respect to the signal, i.e. compare the mean ensemble spread (*noise*) with the average time variability of the ensemble mean (*signal*), the signal-to-noise ratio (Figures A.9 - A.14) needs to be considered. Note that it corresponds to the reverse of the mean normalized ensemble spread, where the normalization is the standard deviation of the ensemble mean (see Section 3.3).



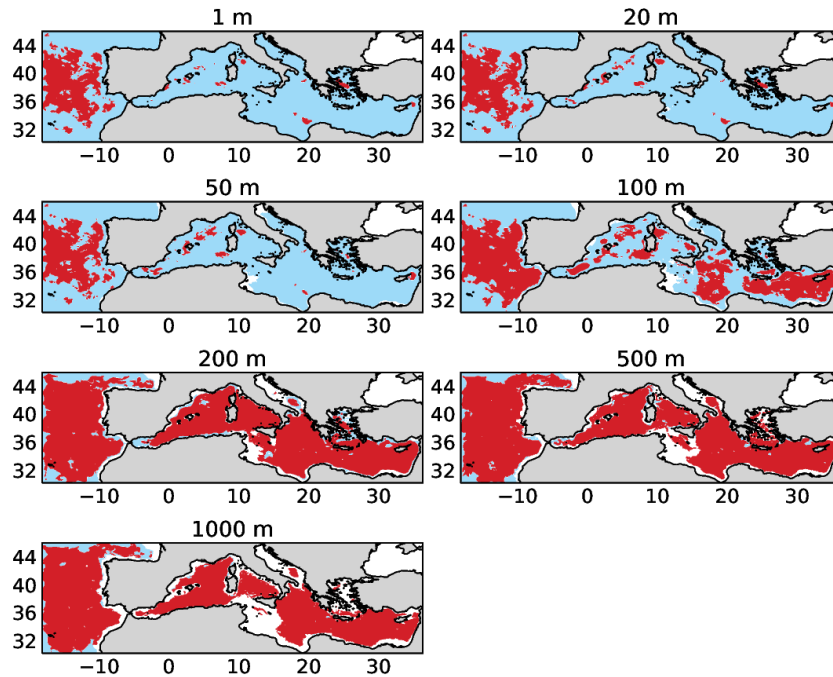


Figure 4.3: In red the points where the signal-to-noise ratio is smaller than 1, i.e. the noise is greater than the signal, for temperature at different depth levels for JAS (top) and JFM (bottom).

First, from Figures 4.3 - 4.5, the net importance of the noise is shown: red points correspond to areas where the signal-to-noise ratio is less than unity, i.e. the noise dominates. For temperature, the signal is dominant in approximately the first 50 m, while the noise thrives from the depth of 100 m. Moreover, for intermediate depths (50 - 100 m) the signal is stronger in winter with respect to summer, since during JFM the noise, mostly confined to the Western Mediterranean, maintains its pattern constant up to 50 m. For salinity, instead, the noise tends to be dominant at all depth levels, even at the surface, except for the Gulf of Lion, the Northern Adriatic Sea, the Sicily Channel and the Aegean Sea in the superficial layers. In summer, the signal is predominant also in the Levantine Sea. Lastly, a similar behaviour is found for the current velocity: the noise thrives at all depths, apart from the Adriatic Sea, the Sicily Channel and the Gibraltar Strait at the surface in both seasons.

Overall, it is evident that, by comparing the signal-to-noise ratio maps (Figures A.9 - A.14) with the corresponding ones of the ensemble spread, the noise thrives at depths over 100 m, even though its module is greater in the superficial layers (in particular in the first 20 m). The areas of larger signal-to-noise

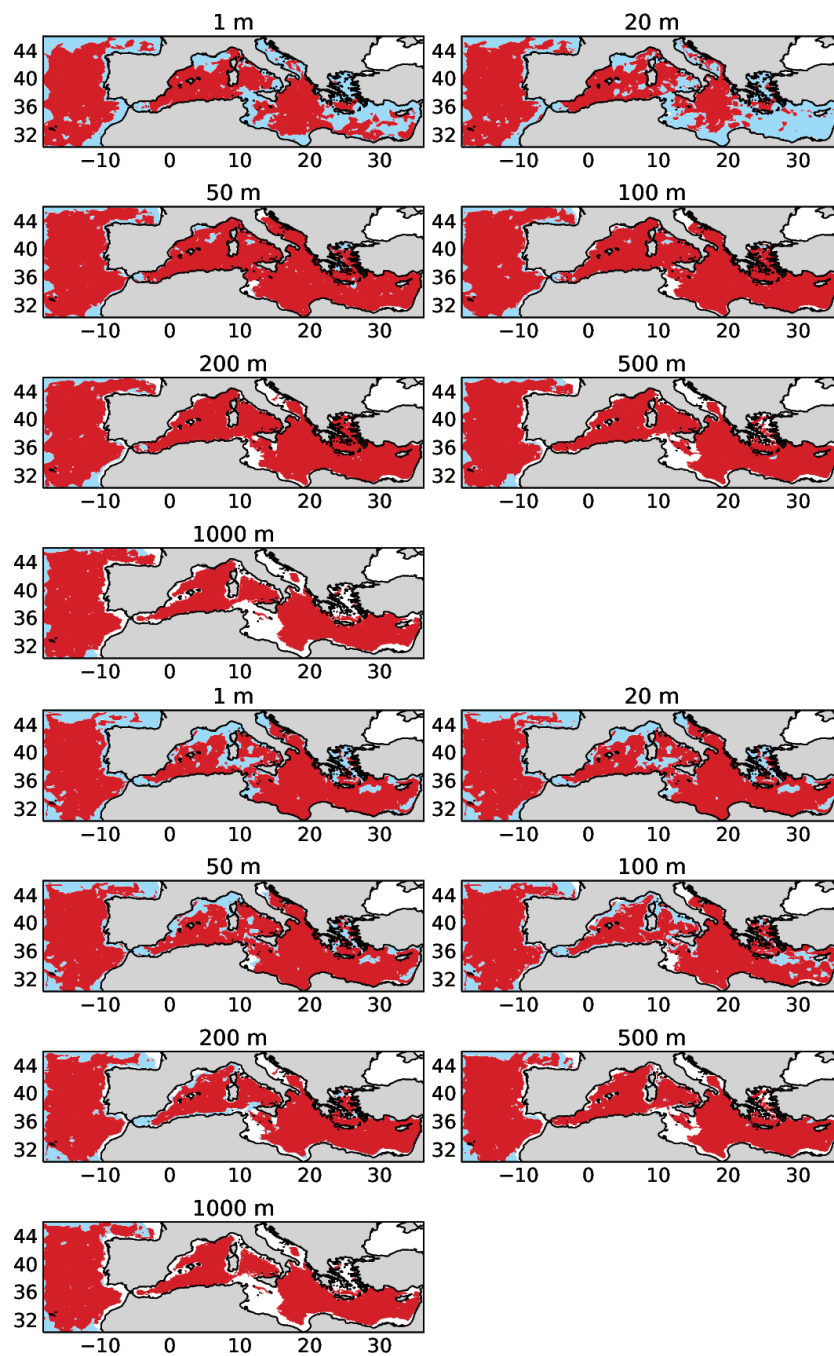


Figure 4.4: In red the points where the signal-to-noise ratio is smaller than 1, i.e. the noise is greater than the signal, for salinity at different depth levels for JAS (top) and JFM (bottom).

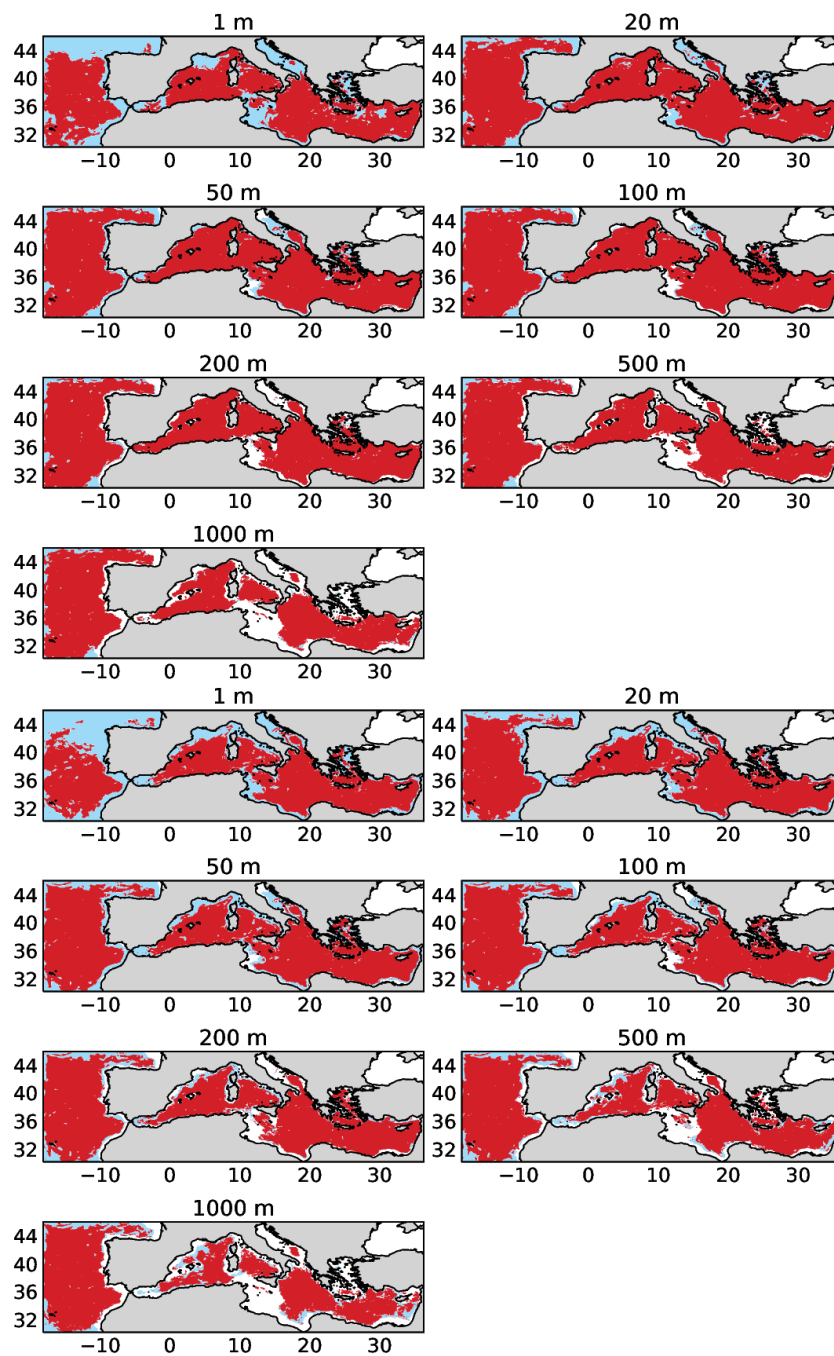


Figure 4.5: In red the points where the signal-to-noise ratio is smaller than 1, i.e. the noise is greater than the signal, for current velocity at different depth levels for JAS (top) and JFM (bottom).

ratio (> 6) correspond to regions of smaller ensemble spread, i.e. the noise is particularly weak in those regions where the signal is significantly stronger. Moreover, the Adriatic Sea and the area offshore from Tunisia and Libya are regions of higher S/N for all variables, while being the shallowest areas in the Mediterranean basin, except for coastal areas, hence the atmospheric forcing is particularly effective in those regions.

For temperature, since the S/N is greater than 1 almost everywhere up to the depth of 50 - 100 m, the maximum of the ensemble spread that was found at 20 m in summer corresponds to a signal-to-noise ratio greater than 1 almost over the entire basin. Furthermore, the S/N is greater in summer. For salinity and current velocity, the locations of the highest S/N are the Adriatic Sea in the proximity of the Po delta, the Aegean Sea and the Gulf of Gabès.

Furthermore, the basin average of the *noise-to-signal ratio* for each variable and for both season is displayed in Figure 4.6. The choice of considering the N/S instead of the S/N is purely motivated in this case by the need of a better visualization. It is evident that the N/S is greater in summer than in winter, after 10-20 m depth, and tends to increase with depth starting from about 0.3 and 1.5 for temperature and salinity respectively, whereas it reaches a maximum (about 2.5) at 200 m for current velocity and then slowly decreases.

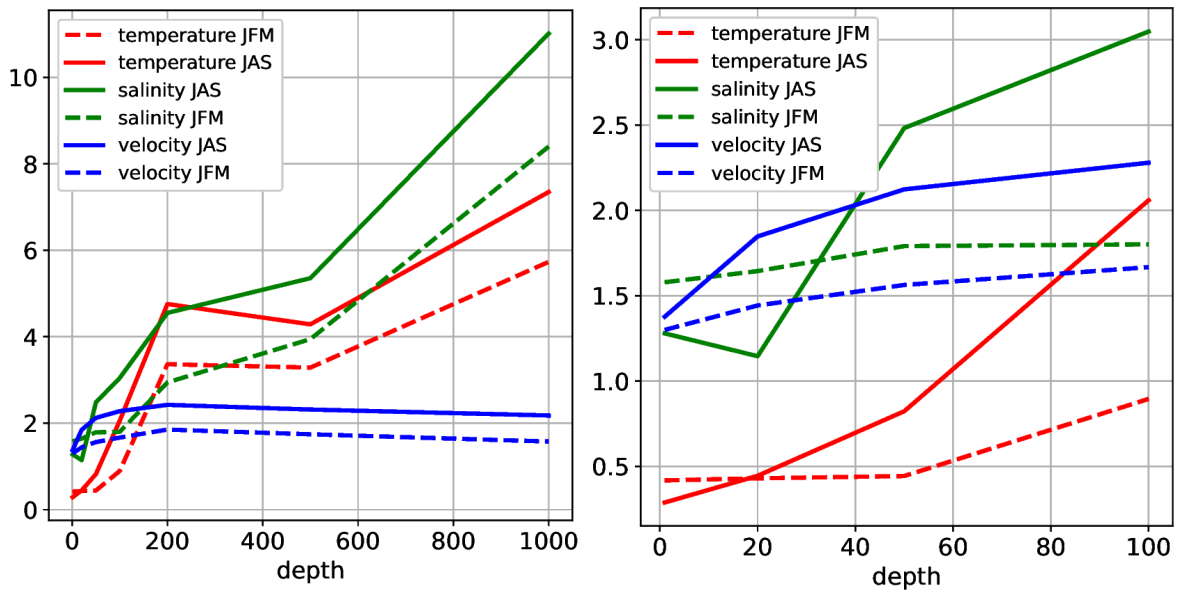


Figure 4.6: Basin average of the N/S in for temperature (red), salinity (green) and current velocity (blue). Up to 1000 m (left), zoom in the first 100 m in the right. JAS (full line) and JFM (dashed line).

Moreover, for temperature the average N/S reaches unity at approximately 60

m in JAS and at 120 m in JFM, whereas for salinity and current velocity the average N/S is always greater than 1. However, note that these profiles have been computed with only 7 depth levels that, even though are significantly representative of the vertical trend, need to be integrated with all the available depth levels, in order to increase their accuracy.

4.4 Relation with the gradients of the fields

In order to investigate the physical reason behind the area and depth distribution of the ensemble spread and of the S/N, a comparison with the mean horizontal and vertical gradients of the variables under study and with the mixed layer depth (Figure A.15) is performed. The idea is to check if a high presence of noise is linked to large spatial variations or high intensity of the field of interest.

As regards the temperature field in summer, the ensemble spread has its maximum below the mixed layer, in the thermocline. This is particularly evident in the vertical profiles of the spread compared with those of the vertical and horizontal temperature gradient in Figure 4.13, where it is clear that the noise peaks right below the mixed layer depth (black horizontal lines). Consequently, the temperature vertical gradient (that almost coincides with the density gradient) has a similar trend and the same peak at 20 m - 30 m with respect to the ensemble spread profile along the vertical column at the 7 chosen locations, even though in the mixed layer the two curves are not always in a good accordance. Furthermore, also the horizontal gradient, that has its peak at the same depth, has a profile similar to the one of the noise especially in the superficial layers, thus implying a coexistence of at least two factors influencing the spread distribution. In fact, by comparing the field of the horizontal temperature gradient, or equivalently the horizontal advection field ($\mathbf{u}_h \cdot \nabla_h T$), with the spread at the surface a very good agreement is found, meaning that the regions with higher spread corresponds to areas of higher horizontal gradients (or stronger horizontal advection), while the vertical temperature gradient does not match the noise field there (Figure 4.7).

Instead, at 20 m depth (Figure 4.8) the ensemble spread field has a very similar pattern to the vertical temperature gradient at the same depth. In fact, the depth of 20 m in summer corresponds, in most part of the basin (see the mixed layer depth field in Figure A.15), to the thermocline. The only exception is the Adriatic Sea, where the spread is small but the vertical gradient is strong. This could be caused by the presence of a very strong signal there, as seen in the previous section, that modulates the noise that would have been present in the absence of the strong atmospheric forcing. At the other depth

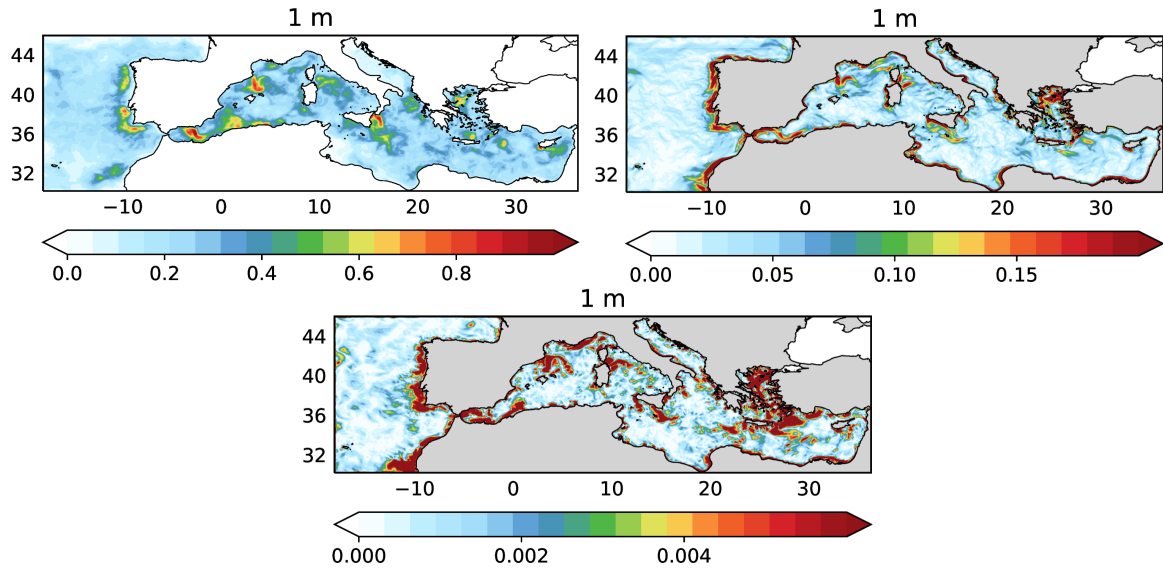


Figure 4.7: Seasonal average (JAS) of the noise (left) at the surface, of the temperature horizontal gradient (right) and of the horizontal advection field (bottom) at the same depth.

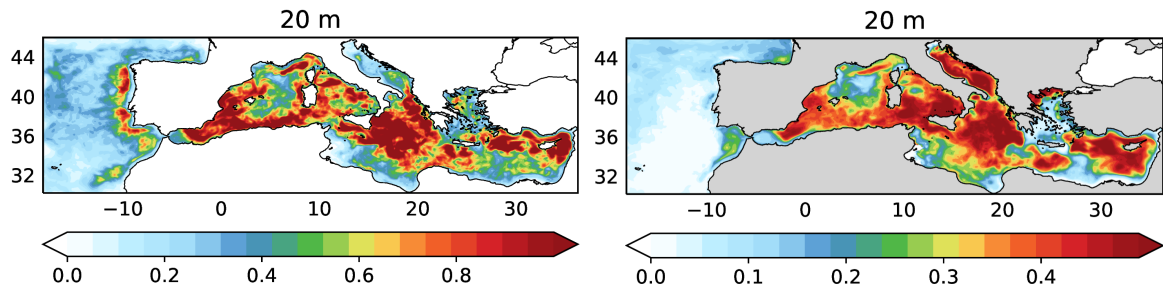


Figure 4.8: Seasonal average (JAS) of the noise (left) at 20 m and of the temperature vertical gradient (right) at the same depth.

levels, the role of the two gradients is not immediately distinguishable as in the superficial layers and the two seems to contribute similarly to the noise, depending on which one predominates at each location. Particularly interesting is the case of the WMed where the spread accurately follows the vertical gradient, both for temperature and salinity, showing a peak at around 100 m, apart from temperature in summer where it reaches its maximum at about 20 m, below the mixed layer. This agreement is probably due to the presence at the depth of about 100 m of the boundary between the flow of AW entering the basin and the opposite one of MW exiting it, which are water masses characterized by very different temperature and salinity values (see Section 2.3).

On the other hand, for the cold season, no clear relation with the gradients was found, as can be deduced by Figure 4.13. The vertical profiles of the noise and of the two gradients are independent one from the other right below the mixed layer, whereas a good agreement is found only with the vertical temperature gradient at depths greater than 100 - 150 m at the locations EMed, LIW, CIW and WMed and with the horizontal temperature gradient in the mixed layer.

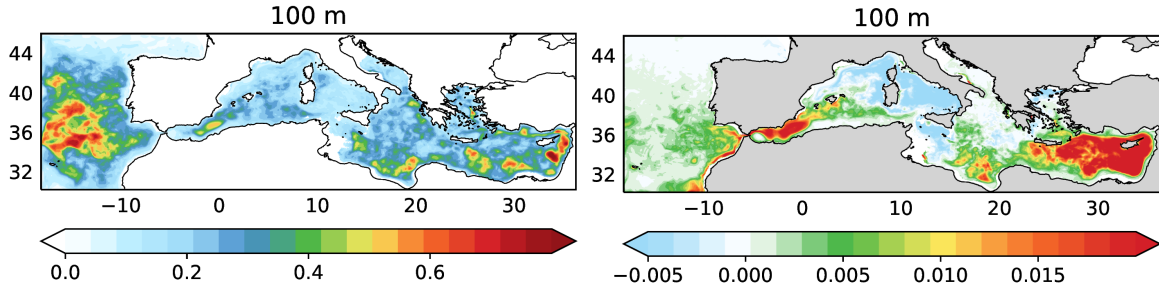


Figure 4.9: Seasonal average (JFM) of the noise (left) at 100 m and of the vertical advection of temperature (right) at the same depth.

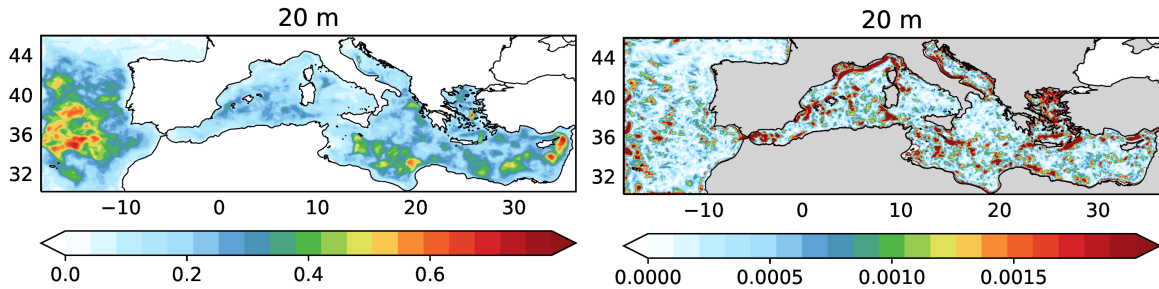


Figure 4.10: Seasonal average (JFM) of the noise (left) at 20 m and of the horizontal advection of temperature (right) at the same depth.

Moreover, a correspondence between the spread field and the vertical gradient (or vertical advection) is found only at 100 m and below (Figure 4.9), whereas at shallower depth a better match is found with the horizontal advection, apart from those regions such as the Gulf of Lion and the Adriatic Sea where the signal is particularly strong. However, this reasoning is definitely not as accurate as the one for summer. It could be because the vertical temperature gradient in winter does not have a defined structure as in the case of summer and it is of one order of magnitude smaller. Thus, its contribution to the ensemble spread is not as significant and easily identifiable as in the warmer months. However, it is to be noted that the Eastern Mediterranean, which

is the regions with higher spread values in winter, is also the warmer area during the cold season.

For salinity, a good agreement is found between the vertical profile of the noise and the horizontal salinity gradient (Figure 4.14), particularly in summer. However, at some locations the vertical salinity gradient is more in accordance, such as at the WMed in summer. Nevertheless, the horizontal salinity gradient accurately reproduces the field of the ensemble spread in both season and at all depths (Figures A.4 - A.5). Consequently, high spread regions accurately correspond to areas where salinity horizontal gradient is greater, due to the presence of rivers that flow into the Mediterranean Sea, such as the Ebro, the Po, the Rhone and the Nile, and of water inflow through the Gibraltar Strait and the Dardanelles. Again, the Adriatic Sea, the Gulf of Gabès and the Gulf of Lion, even if they are characterized by a high horizontal salinity gradient, they show little noise, probably due to the presence of the strong signal in those regions.

Finally, as regards the current velocity, a good match is found with the ensemble mean (Figures A.6 - A.7), i.e. the average horizontal current velocity field: the higher the current velocity, the greater the ensemble spread in both season. Moreover, the ensemble mean is the only factor able to explain the spread pattern, which maintains itself constant along the vertical column, while decreasing its intensity. To show this, the ratio between the intensity of the horizontal current velocity and its corresponding ensemble spread is reported in Figure 4.11: their ratio is constant all over the basin except for the Northern Adriatic Sea, the Gulf of Gabès and, especially in winter, the Gulf of Lion, which are regions characterized by a large S/N ratio. Thus, strong oceanic currents are linked to a large presence of noise except for those regions of great influence of the atmospheric forcing.

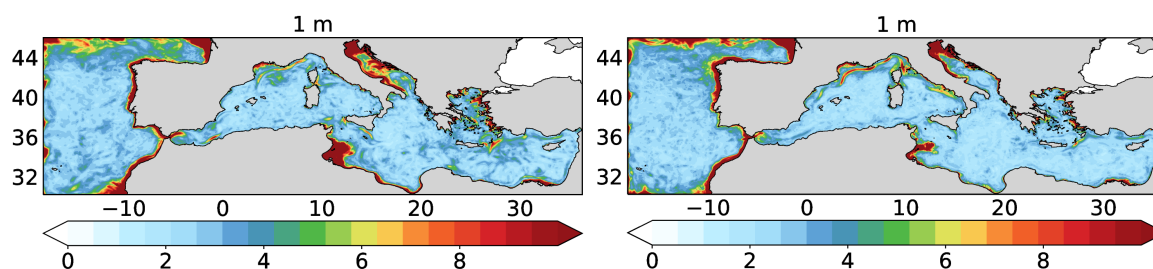


Figure 4.11: Ratio between the average horizontal current velocity field and the corresponding ensemble spread at the surface for JAS (left) and JFM (right).

In order to verify if these findings are valid only for the examined year of 2021,

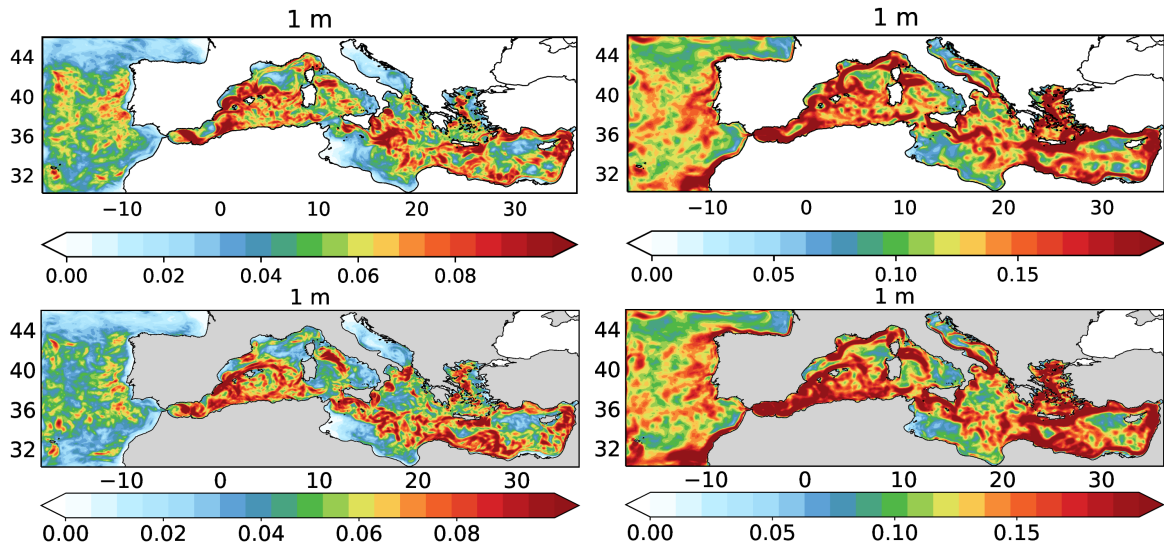


Figure 4.12: Ensemble spread relative to current velocity (left) and the field of current velocity itself (right) in JAS at the surface, relative to the year 2021 (top) and 2020 (bottom).

the same analysis is reproduced for the year 2020 with only four of the five used simulations. Thus, the results are confirmed also for 2020 as regards the pattern of the noise itself (and of the S/N), its seasonality and its relation to the gradients or to the current intensity: the spread has the same distribution in 2020 and in 2021, apart from some small-scale differences, and it is in good agreement with the previously found quantities, depending on the chosen variable. Furthermore, these differences are easily explained by the variations in the fields of the gradients of temperature and salinity or in the mean current field between 2020 and 2021. All the results relative to the year 2020 are not reported here since it would be redundant, but as an example the spread for the current velocity at the surface in summer and the corresponding current field are shown for both years in Figure 4.12.

In conclusion, the noise relative to temperature in summer is related to both the horizontal temperature gradient, mainly at the surface, and the vertical temperature gradient, predominantly at the thermocline, whereas no clear and definite pattern is found for the winter season. For salinity, the noise is linked to the intensity of the horizontal salinity gradient at all depths and in both season, whereas for current velocity the same relation is deduced between the noise and the ensemble mean. The link between the ensemble spread (or the uncertainty) relative to a certain field and the gradient of the same field can be easily understood: small differences among the simulations

in those regions are amplified by the large variations of the field there, e.g. small displacement of a water particle at the thermocline implies a greater modification of the temperature values with respect to the same displacement in the abyssal layer. Consequently, the noise is greater where strong gradients are at play: for temperature is mainly at the thermocline in summer, when it is particularly pronounced, whereas for salinity, being mostly advected in the horizontal direction, is found in correspondence with high horizontal variations due to water inflow and outflow. These results are in accordance with what found in previous studies (Adani et al [20] - Pinardi et al [21]): the uncertainty in ocean simulations is greater in the presence of strong variability probably due to the inaccurate representation of the thermocline formation processes and of the advective processes that move the AW around the basin. On the other hand, for current velocity the uncertainty of the field is linked to the strength of the field itself, meaning that regions with stronger currents are also those with greater noise. It could be due to the presence of greater energy in those regions and consequently more numerous mesoscale structures, which are sources of noise, as seen in Tang et al [6].

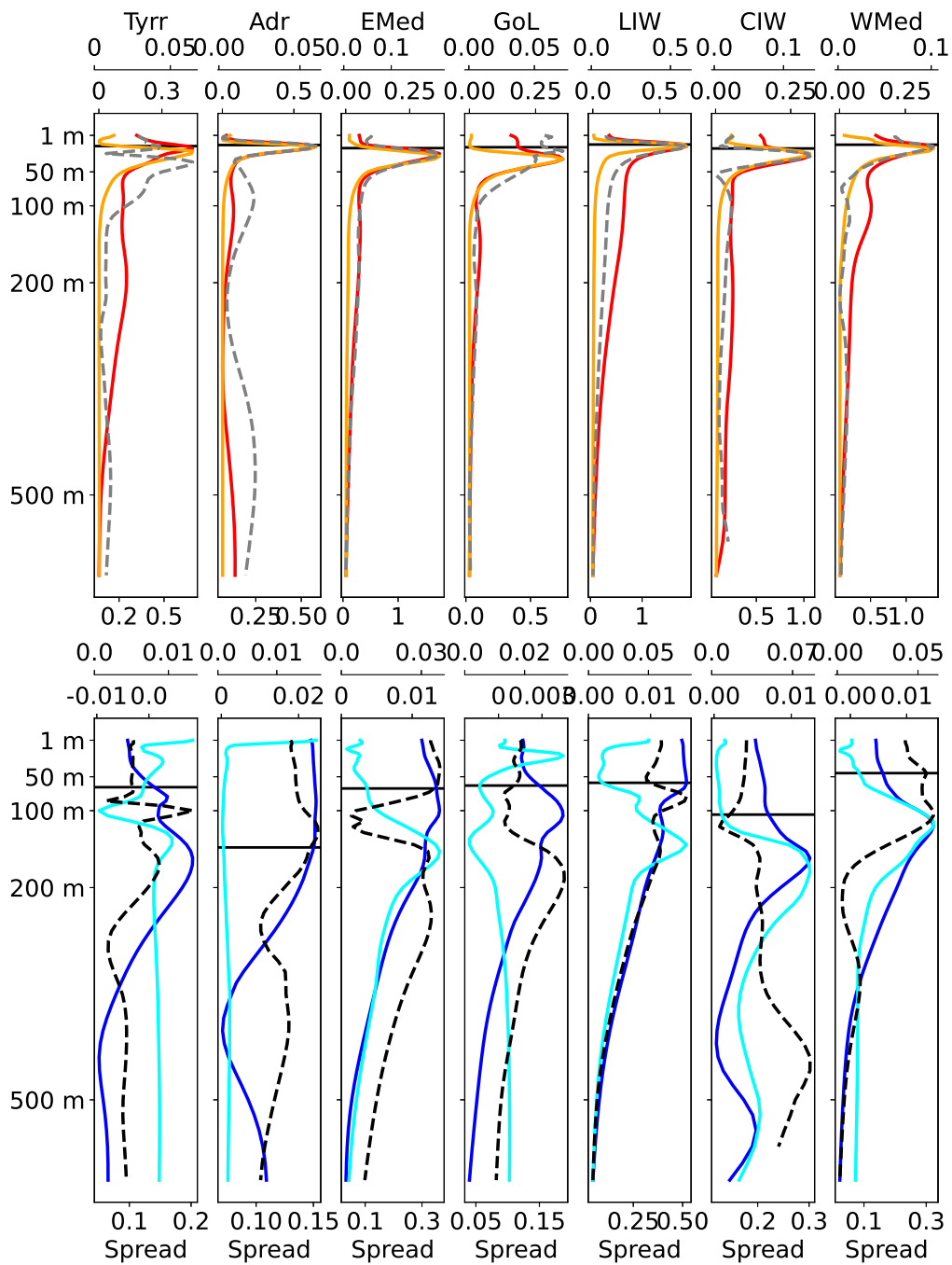


Figure 4.13: Vertical profile of the ensemble spread for temperature (red/blue) versus the vertical (yellow/cyan) and the horizontal (grey/black dashed line) temperature gradient at the seven chosen locations. August mean (top), February mean (bottom). The horizontal black line indicates the mixed layer depth.

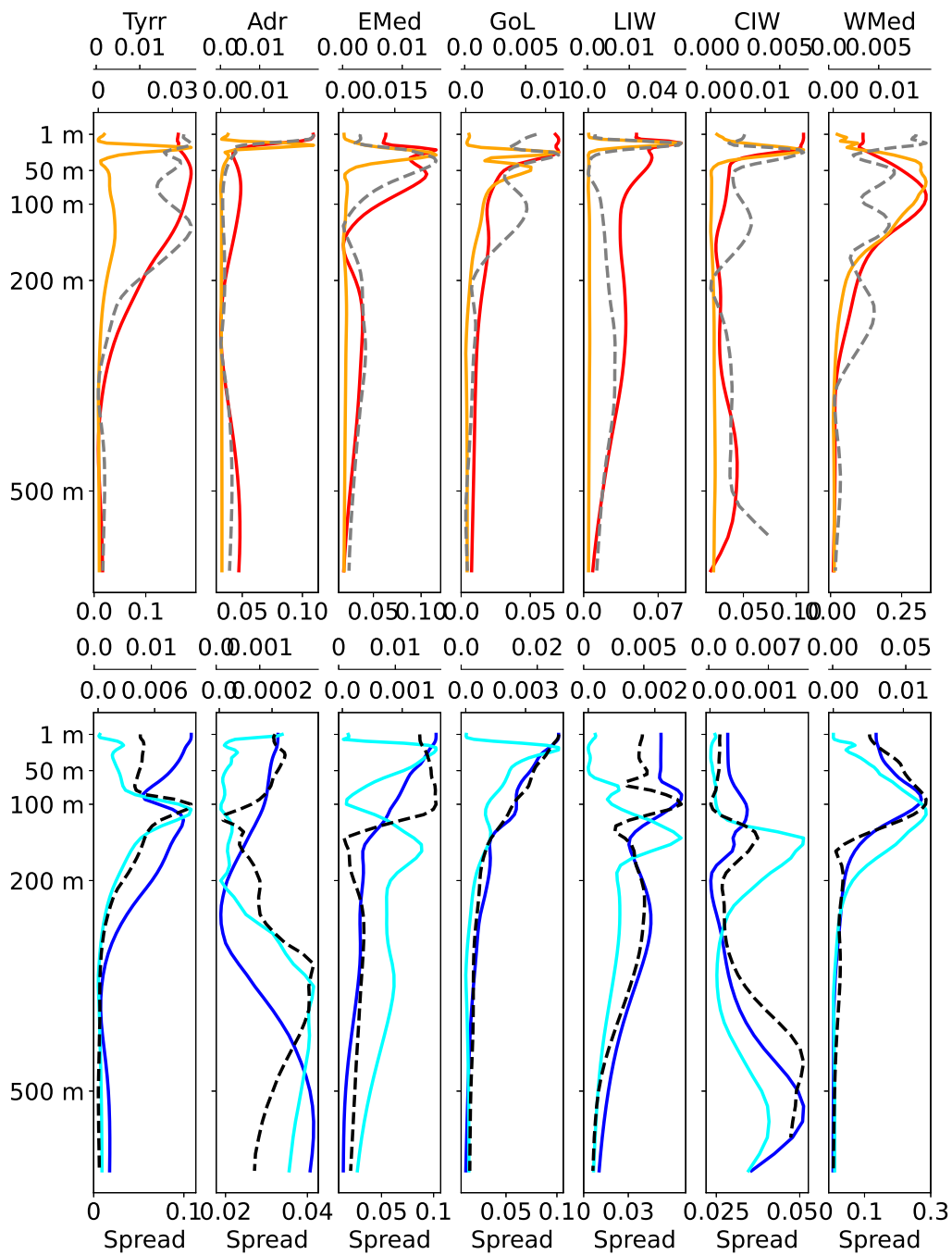


Figure 4.14: Vertical profile of the ensemble spread for salinity (red/blue) versus the vertical (yellow/cyan) and horizontal (grey/black dashed line) salinity gradient at the seven chosen locations. August mean (top), February mean (bottom).

4.5 Preliminary analysis on the decorrelation time scale of the simulations

Due to the differences qualitatively found in the time series (Figures A.1 - A.2) between the multi-year ensemble spread and the single-year ensemble spread, a preliminary study aiming at quantifying this disagreement is carried out. First, the basin average at different depth levels of the ensemble spread and of the N/S are computed for both season and for both ensembles (Figure 4.16). It is clear that the multi-year ensemble determines an ensemble spread and a noise-to-signal ratio that are always greater than the ones derived from the single-year ensemble, apart for the current velocity for depths greater than 400 m.

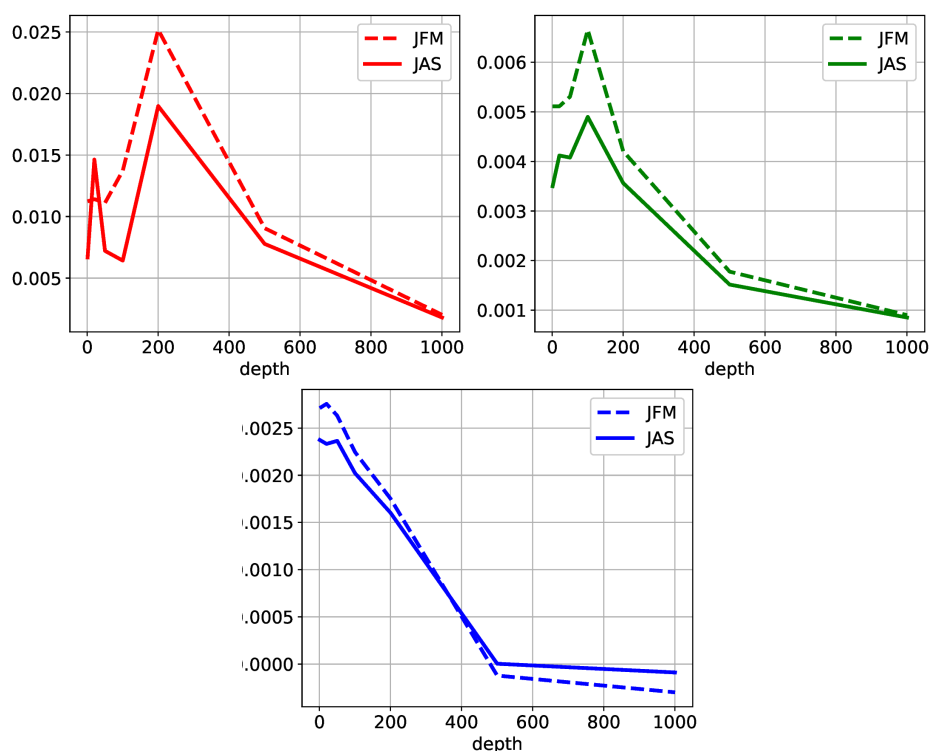


Figure 4.15: Basin average of the difference between the multi-year ensemble spread and the single-year ensemble spread for temperature (red), salinity (green) and current velocity (blue).

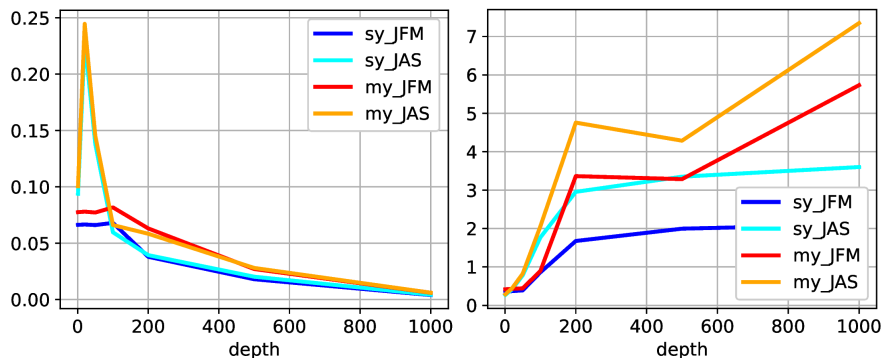
The two spreads show a greater difference (Figure 4.15) in JFM and tend to zero after about 400 m. For temperature, the spread difference has a peak at 200 m in both season (around 0.02°C) and a relative maximum at 20 m m for

JAS ($0.015\text{ }^{\circ}\text{C}$). As regards salinity, the maximum difference (around $0.005\text{-}0.007\text{ }10^3\text{ ppm}$) is at 100 m in both season, whereas for current velocity the difference has its maximum at the surface or at 20 m (around 0.0025 m/s). The profile found before for the N/S (see Section 4.1.3) is confirmed also from the single-year ensemble in the case of current velocity, whereas, for temperature and salinity, the growth with depth seen for the multi-year ensemble spread is much more confined in the case of the single-year ensemble spread, stabilizing itself around the value of 4 in JAS and 2 in JFM. However, both ensembles, apart from the superficial layers, show greater values of the N/S in summer with respect to winter. As regards the ensemble spread, both ensembles are characterized by the same trend, showing greater values in summer for the scalar quantities and in winter for the current velocity. Overall, the noise tends to decrease with depth, apart from the case of temperature and salinity in JAS where both ensembles predict a peak at 20 m depth.

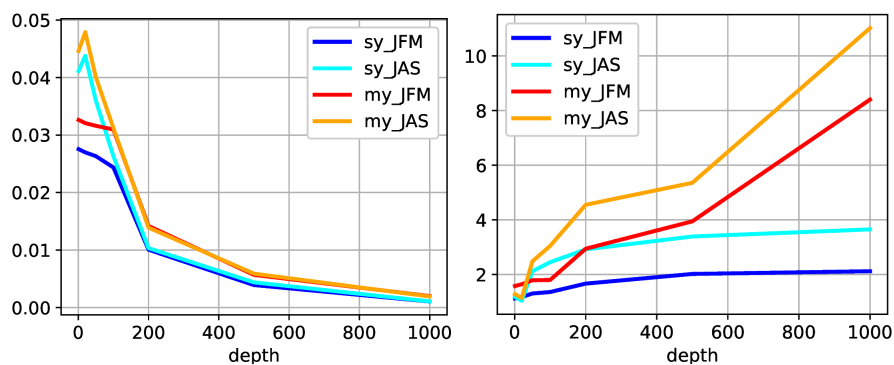
As a further analysis, the ratio between the two ensemble spreads is calculated for the entire basin, showing both regions where one is greater than the other and viceversa.

In conclusion, the systematic difference between the multi-year ensemble and the single-year ensemble, such that the spread predicted by the first is greater on average in both season, implies that at least until summer the two spreads are not equivalent, even though the difference decreases in summer. Thus, the simulations of the single-year ensemble remain correlated with each other during the examined period and the threshold of one month assumed in [6] as a decorrelation time scale of the simulations does not seem to be correct: the system still remembers the initial conditions after only one month and a longer period, probably of the order of one year and at least of six months, is needed. However, the determination of the exact time scale is beyond the scope of this work and further analyses are needed in order to accurately determine the time scale of predictability of the system.

Spread and N/S - Temperature



Spread and N/S - Salinity



Spread and N/S - Current velocity

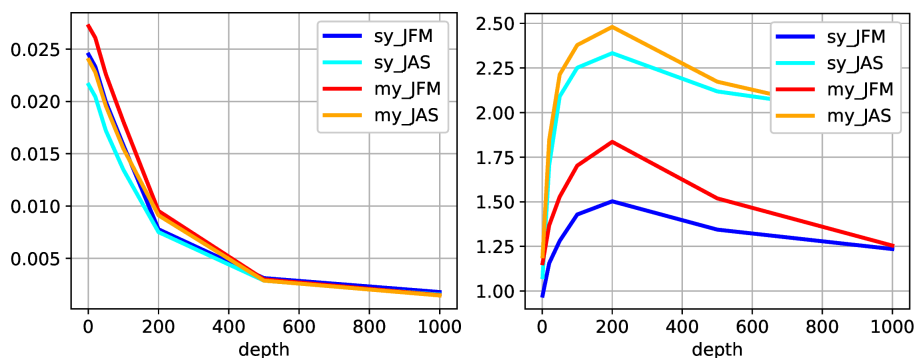


Figure 4.16: Basin average of the ensemble spread (left) and N/S (right) relative to temperature (top), salinity and current velocity (bottom) for both season and both ensembles: multi-year ensemble in JAS (orange) and in JFM (red), single-year ensemble in JAS (cyan) and JFM (blue).

CONCLUSION AND FURTHER DEVELOPMENTS

In the present work, through an ensemble of five identical ocean model simulations that differ only in the initial conditions taken at the different start dates, the noise in the Mediterranean Sea relative to the field of temperature, salinity and current velocity was investigated by defining it as the seasonal averaged spread of the ensemble. Its influence on the Mediterranean variability was deduced by comparing it to the corresponding signal, identified as the seasonal averaged variability of the mean of the same ensemble. Thus, its dependence on depth and area was described and a possible explanation for its pattern was found. Overall, the noise for the scalar quantities is higher where there is a greater spatial variability of the quantity of interest, whereas for the current velocity where the mean current itself is stronger.

For temperature, higher values of the spread in summer are localized right below the mixed layer, in the thermocline, where the vertical temperature profile is steeper. Thus, the maximum of the noise averaged over the basin is found at about 20 m depth. However, at the surface the pattern of the noise is in very good agreement with the horizontal temperature gradient instead. On the other hand, in winter the noise is mainly present in the Eastern Mediterranean maintaining itself similar in the first 100 m. As regards salinity in both season, the noise is related to the horizontal salinity gradient, or to the horizontal salinity advection, which is particularly significant in the Alboran Sea and along the coast of Spain, south of the Ionian Sea and along the coast of Libya and in the Aegean Sea. Following the horizontal salinity gradient, in summer the spread is stronger in the superficial layers, while during winter the maximum is found at about 100 m depth. Lastly, the noise for the current velocity is diffused all over the basin, except for the Adriatic Sea and the Gulf of Gabès, following exactly the distribution of the intensity of the current. Moreover, compared to the signal, the noise for salinity and for current

velocity thrives at all depths, even at the surface, whereas for temperature it becomes dominant only after about 50 m (JAS) - 100 m (JFM) depth. Finally, by comparing the ensemble (*multi-year*) with the so called *single-year* ensemble, the decorrelation time scale of the simulations was briefly considered: averaging over the basin, the noise predicted by the multi-year ensemble is always greater than the one from the single-year ensemble in both seasons, meaning that a systematic difference between the two ensembles is present. This implies that, since the simulations from 2020 were initiated between August and December, a time scale of decorrelation of one month, assumed in other studies, does not hold and a longer period of at least six months is necessary.

The link between the noise and the gradients of the corresponding field is explained by the fact that small differences among the simulations are amplified by the large variations that characterize the field there: small displacement of water at the thermocline and at a region of strong horizontal salinity advection entails a greater change in the temperature and salinity field respectively than the modification produced by the same displacement in a more static area. On the other hand, the relation between the noise and the mean current velocity is thought to be caused by a greater presence of energy which implies, through energy cascading, the formation of small scale structures, which seems to be related to the noise (Tang et al. [6]). However, further analysis are needed to confirm these suppositions and to explain why for temperature in winter no clear relation with the gradients was found and the effect of multiple factors seems to need to be considered.

Overall, these results allow for a better identification of the sources of uncertainties in ocean models, which is useful in order to pinpoint those processes and features whose representation needs to be improved in ocean simulations, such as salinity advection processes or eddies' variability. On a more physical level, the present dissertation provided a four-dimensional characterization of the intrinsic variability of the Mediterranean Sea, recognizing its seasonality, its spatial distribution and its importance relative to the atmospheric forcing. Finally yet importantly, the presence itself of noise was shown, meaning that the ocean-variability in the Mediterranean Sea is indeed not only externally determined by the atmospheric forcing, but also internally generated, as expected by stochastic climate theory (see Section 2.1).

However, this study was limited by the relative short time window of two consecutive years, even though the results were confirmed in both of them. One possible improvement would be to consider a longer time period in order to prove that the results are not narrowed down by the chosen years, but holds regardless. Similarly, the present study is confined to the Mediterranean Sea,

thus a comparison with the results for other seas should be considered. Moreover, further analysis are needed as regards the sensitivity of the system on initial conditions, for instance by considering several simulations each one initiated one month before the other, going back at least one year before 2021. In this way, a precise calculation of the time after which the simulations loose correlation would be possible. This would be of both operational and physical importance since it would give information on how to build ensembles to properly study the noise and on the sensitivity of the system on initial conditions. Furthermore, the S/N scale dependency analysis should be performed, both in space and in time, in order to understand at which scales the noise thrives. For instance, an EOF decomposition of the S/N in the Mediterranean Sea should be carried out as done by Tang et al [6] in the South China Sea and the results should be compared, in order to verify if the relation found in the SCS, i.e. the noise dominates at small spatial scales (about 30 km), is confirmed in another basin. Finally, the same analysis should be done in the presence of tides, which were not included in these simulations, to see how the noise behaves when subjected to the additional tidal forcing.

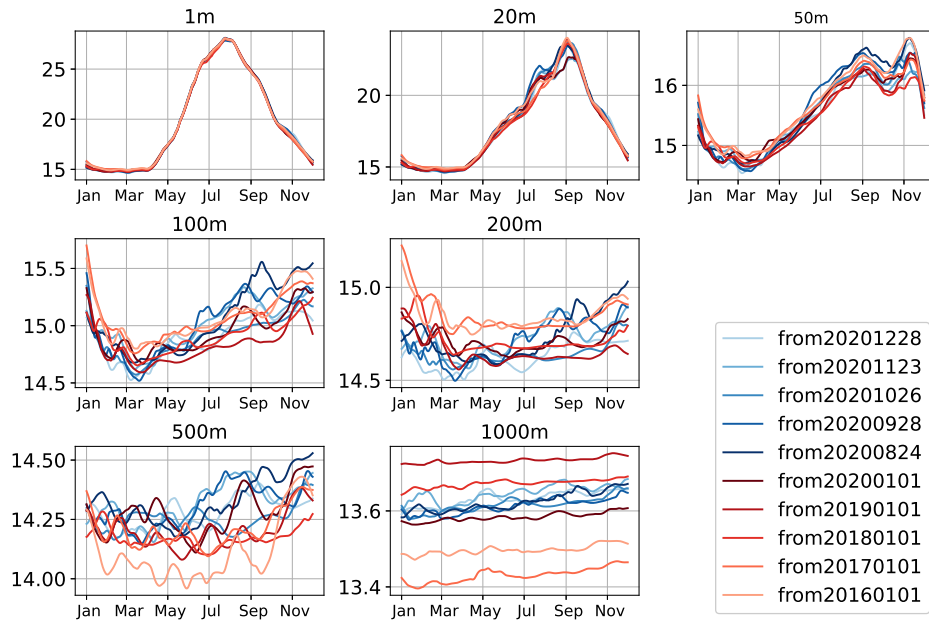
APPENDIX

A

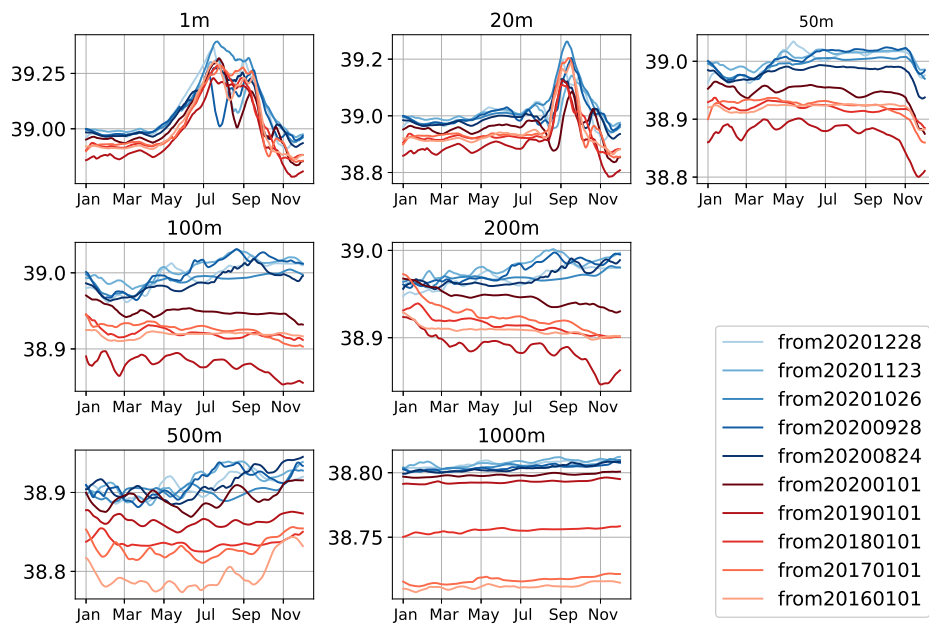
FIGURES

APPENDIX A. FIGURES

Adr - Temperature - Low Frequency



Adr - Salinity - Low Frequency



APPENDIX A. FIGURES

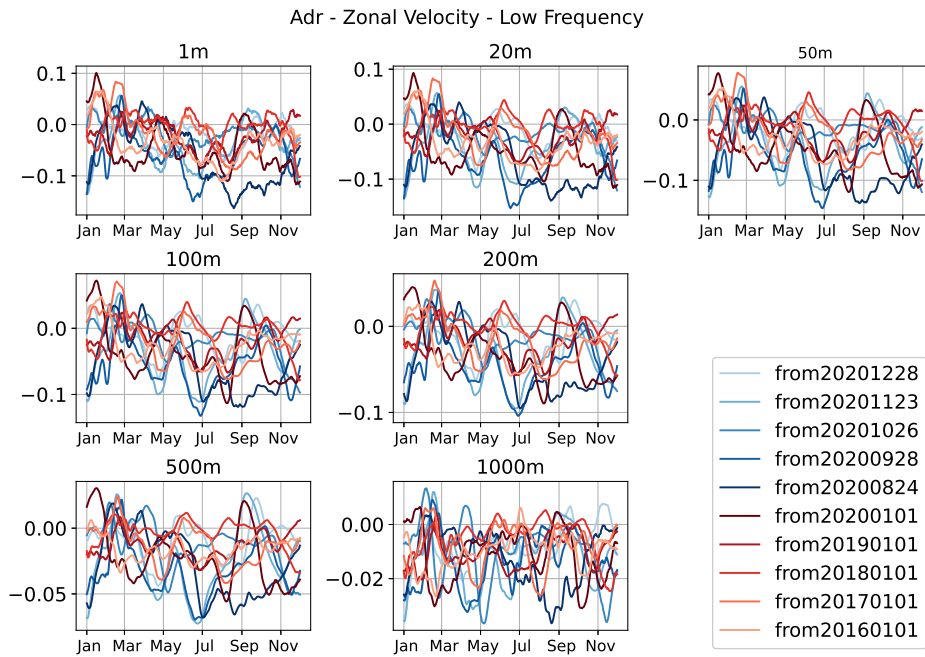
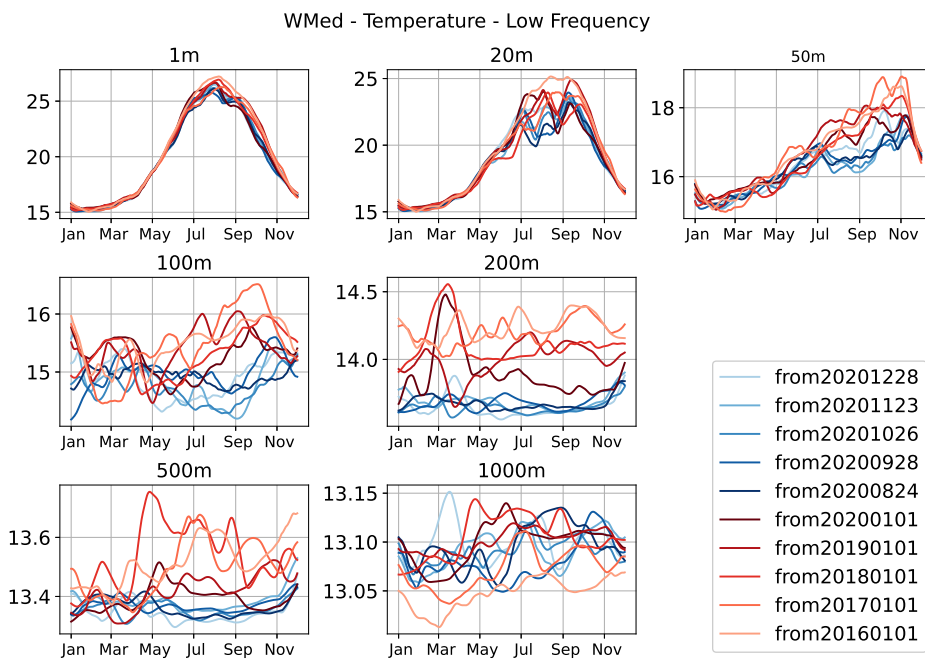


Figure A.1: Low frequency component (> 30 days) of the time-series of temperature (top of previous page), salinity (bottom of previous page) and zonal velocity (here) in the Adriatic Sea *Adr*. In red those of the multi-year ensemble, in blue the members of the single-year ensemble.



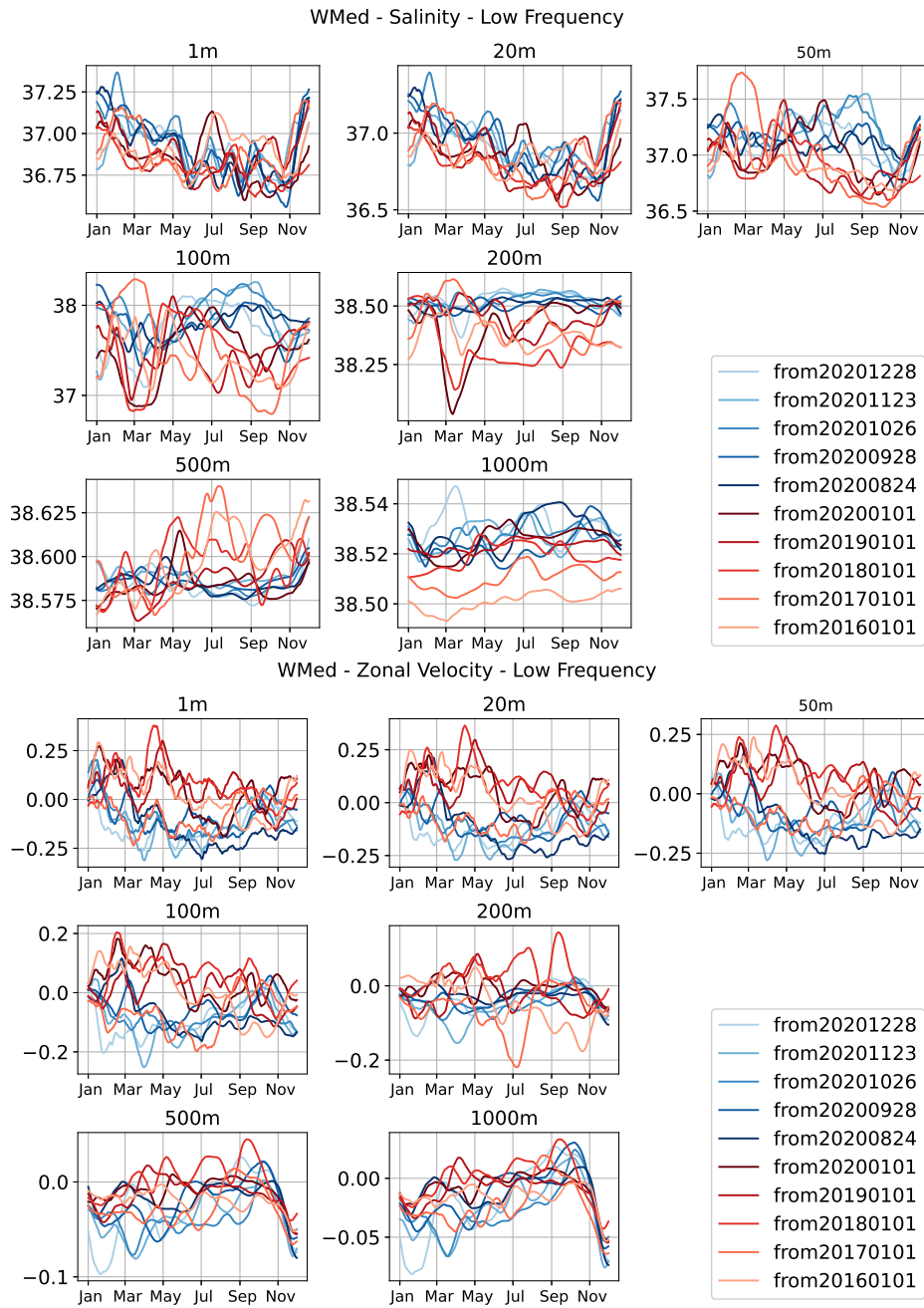


Figure A.2: Low frequency component (> 30 days) of the time-series of temperature (previous page), salinity (top) and zonal velocity (bottom) in the Western Mediterranean *WMed*. In red those of the multi-year ensemble, in blue the members of the single-year ensemble.

APPENDIX A. FIGURES

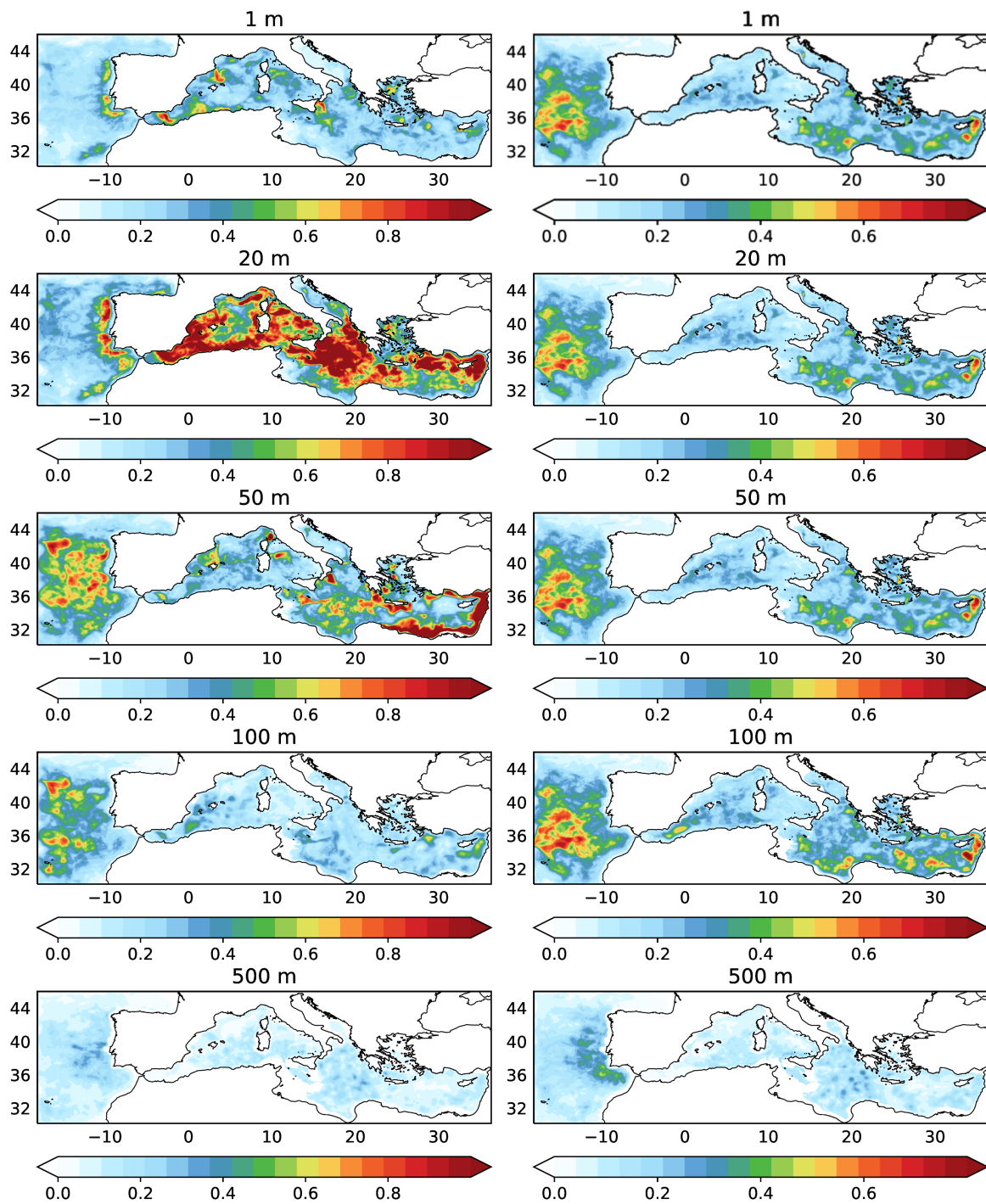


Figure A.3: Temperature (°C) JAS (left) and JFM (right) - Ensemble spread at the depth levels of 1 m (top), 20 m, 50 m, 100 m and 500 m (bottom).

APPENDIX A. FIGURES

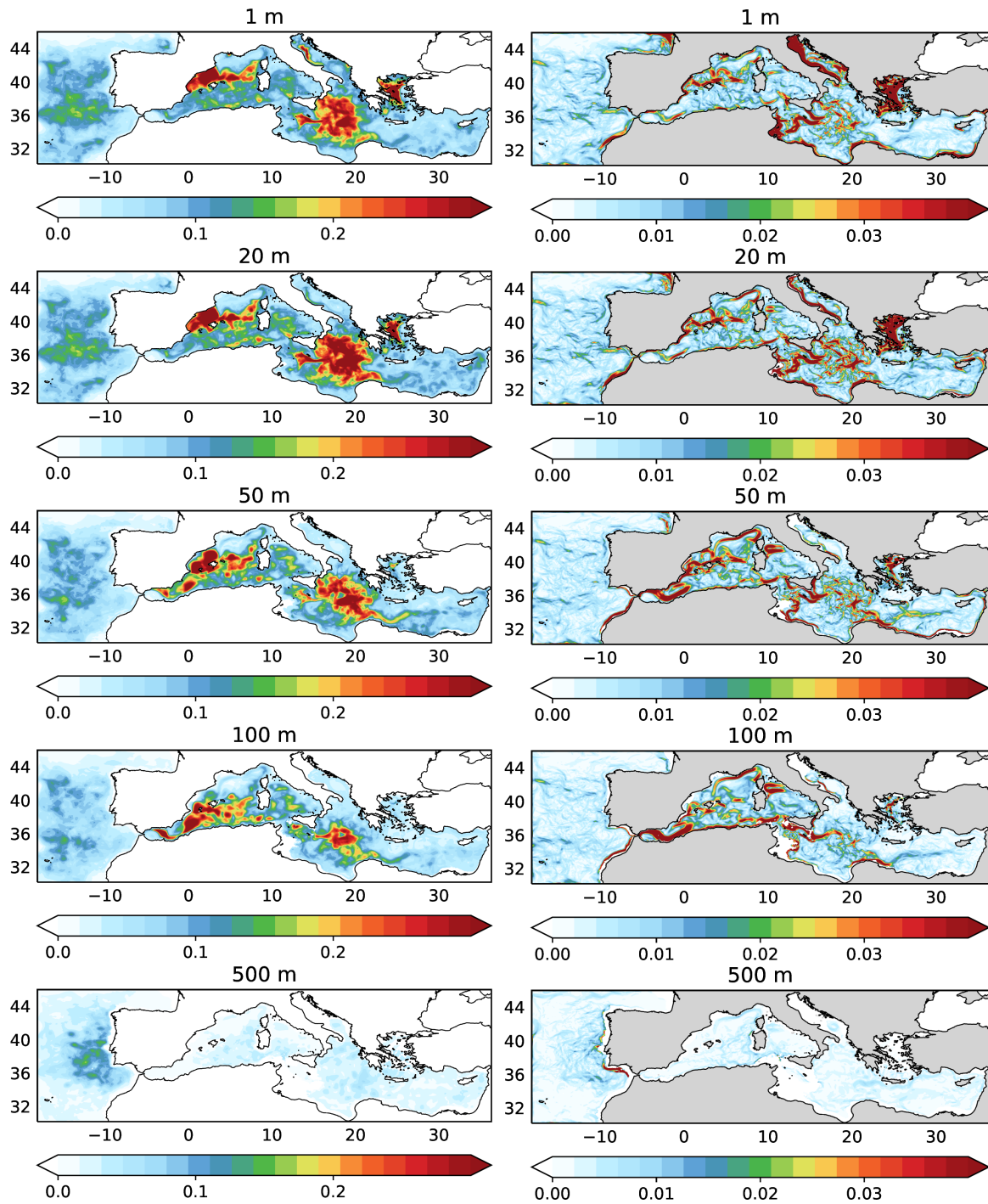


Figure A.4: Salinity (10^3 ppm) JAS - Ensemble spread (left) and horizontal gradient (right) at the depth levels of 1 m (top), 20 m, 50 m, 100 m and 500 m (bottom).

APPENDIX A. FIGURES

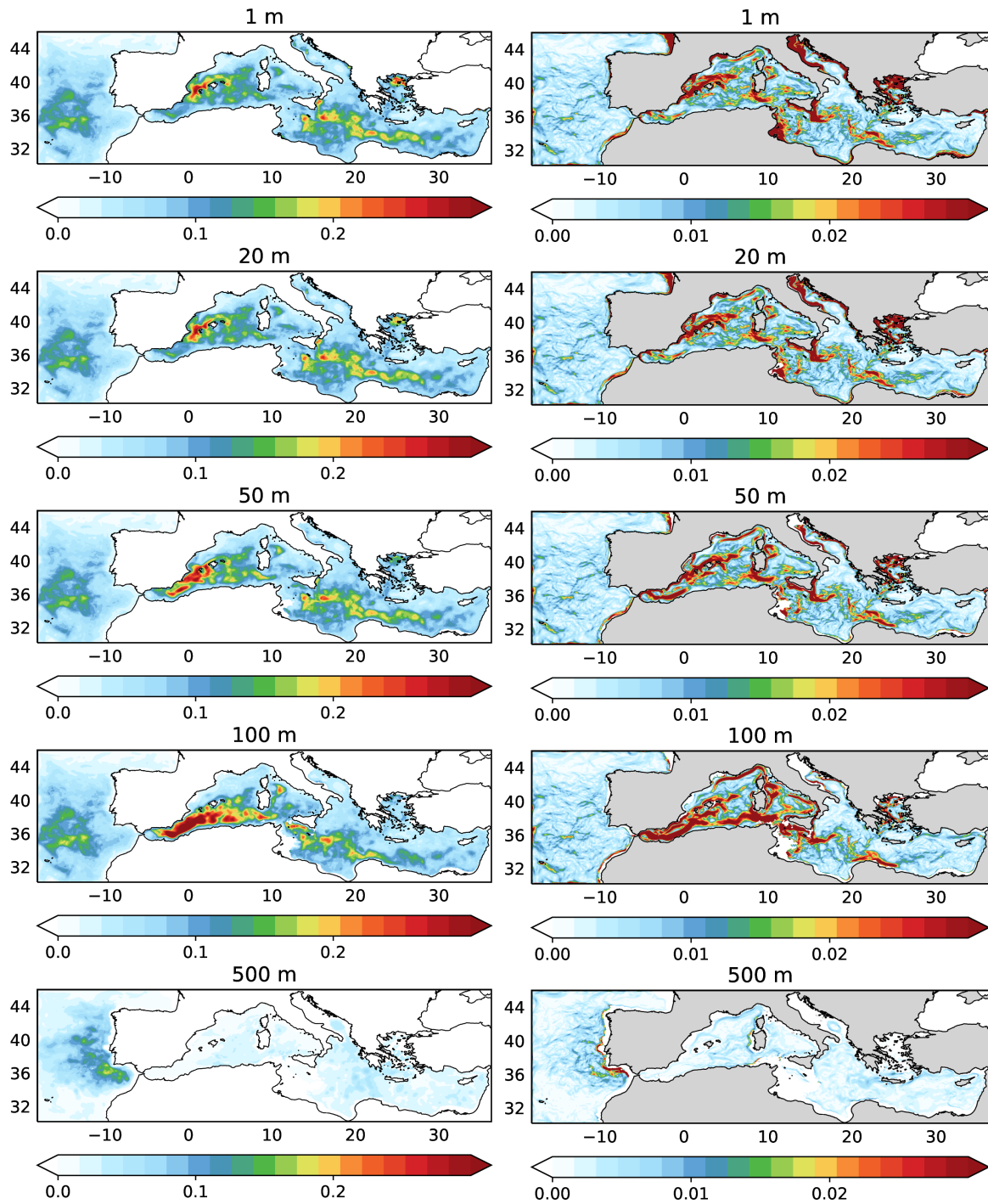


Figure A.5: Salinity (10^3 ppm) JFM - Ensemble spread (left) and horizontal gradient (right) at the depth levels of 1 m (top), 20 m, 50 m, 100 m and 500 m (bottom).

APPENDIX A. FIGURES

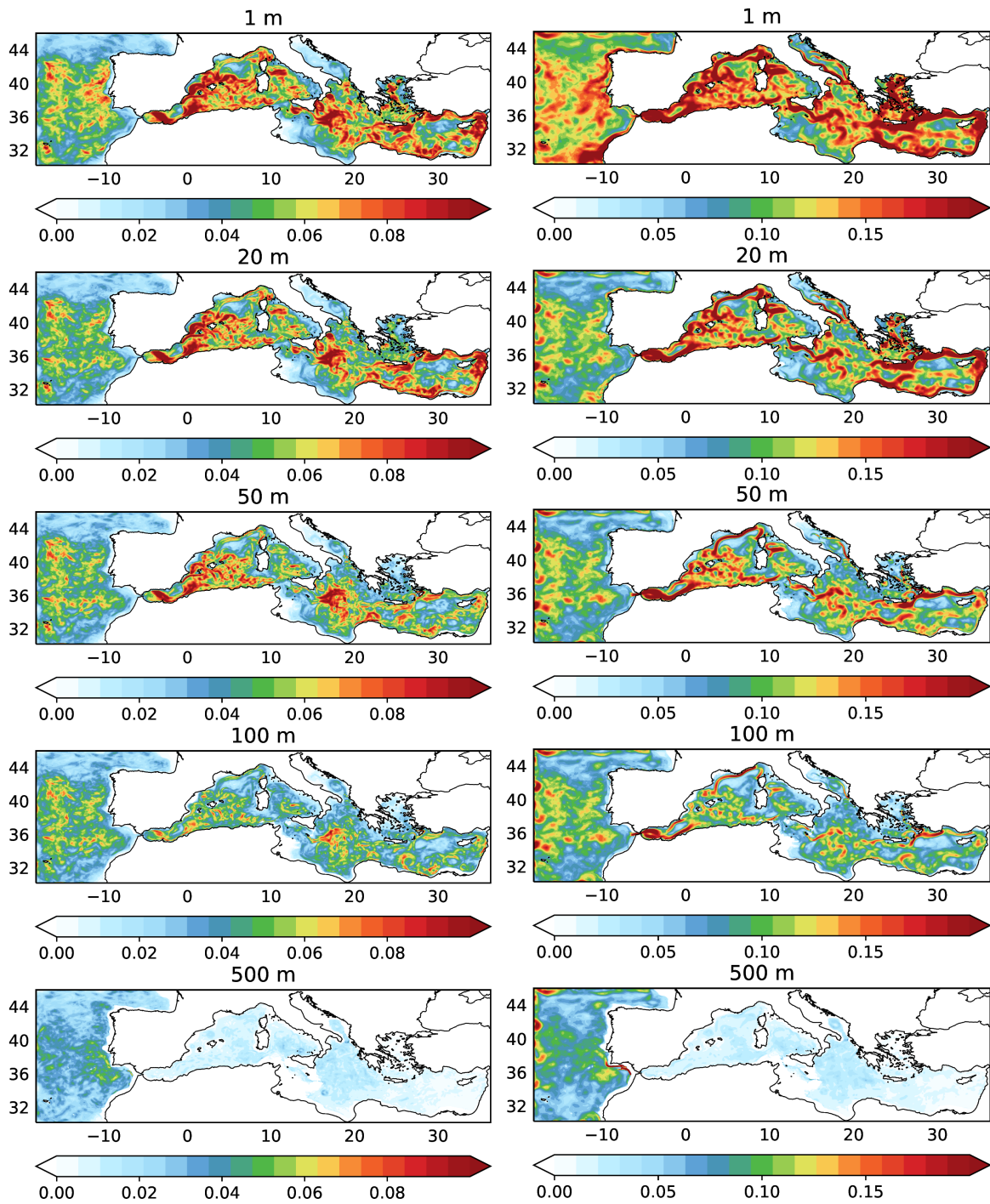


Figure A.6: Current velocity (m/s) JAS - Ensemble spread (left) and ensemble mean (right) at the depth levels of 1 m (top), 20 m, 50 m, 100 m and 500 m (bottom).

APPENDIX A. FIGURES

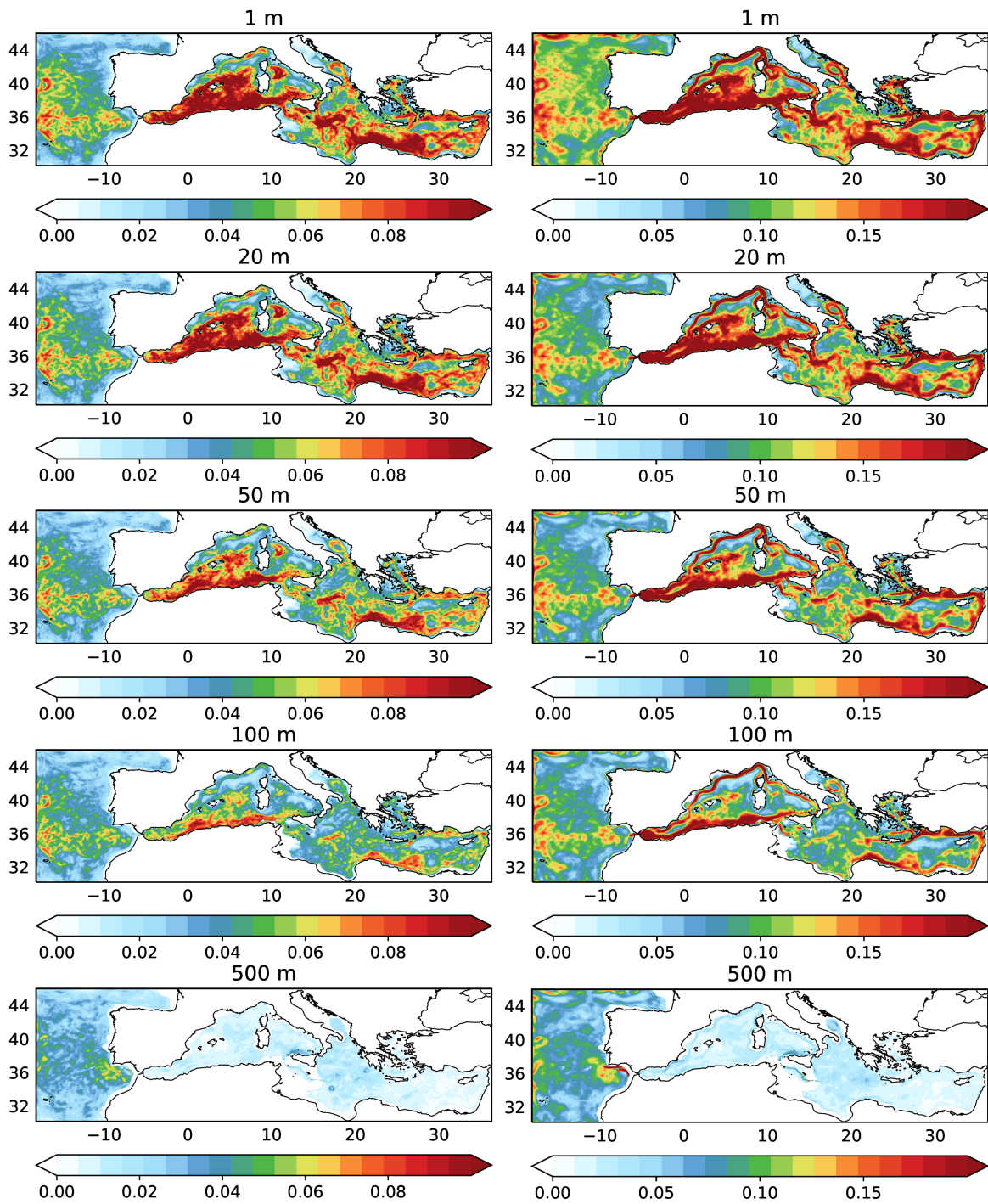
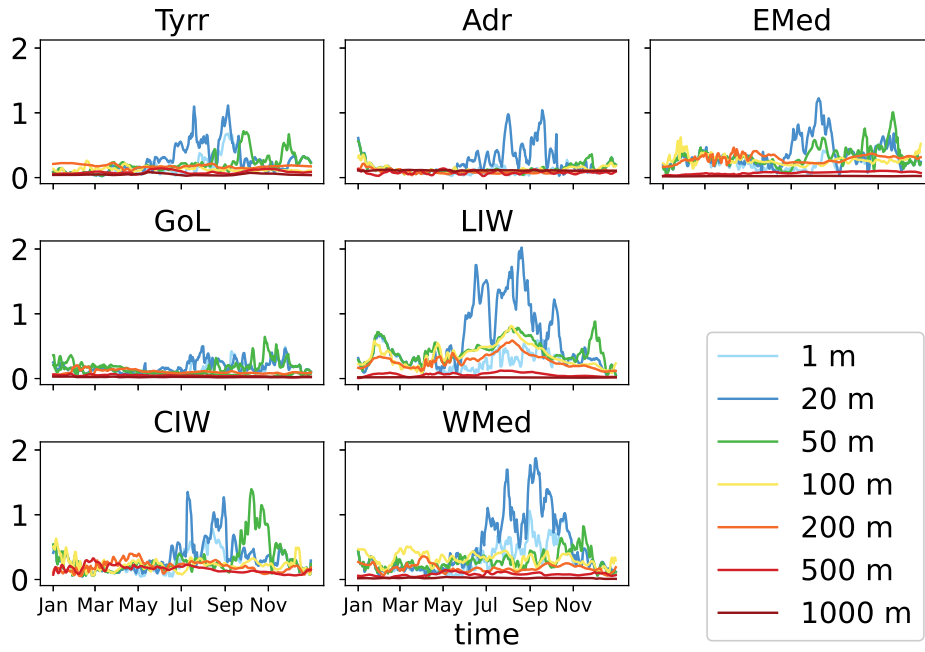
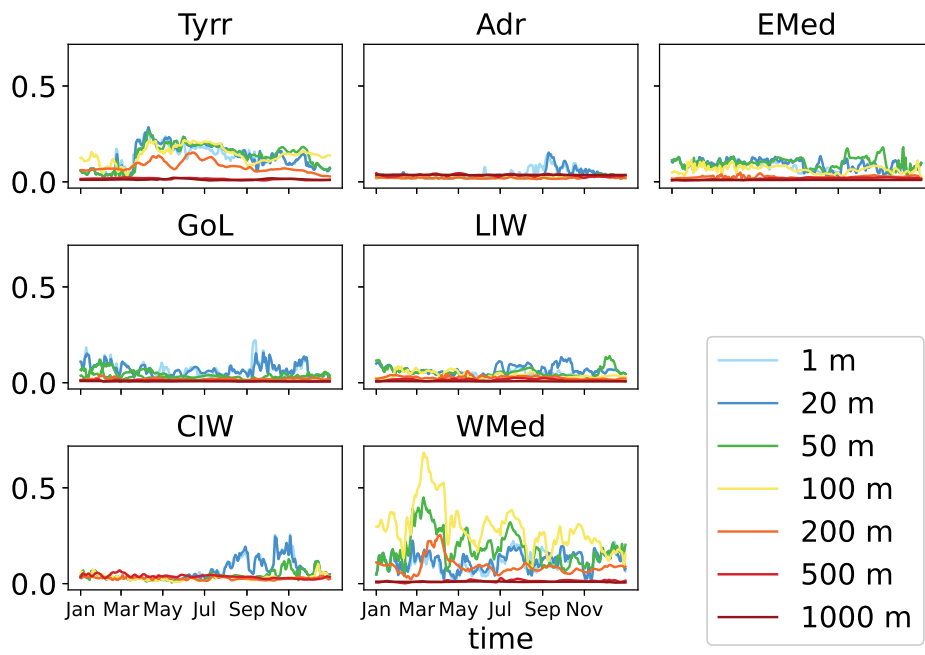


Figure A.7: Current velocity (m/s) JFM - Ensemble spread (left) and ensemble mean (right) at the depth levels of 1 m (top), 20 m, 50 m, 100 m and 500 m (bottom).

Temperature - Ensemble spread



Salinity - Ensemble spread



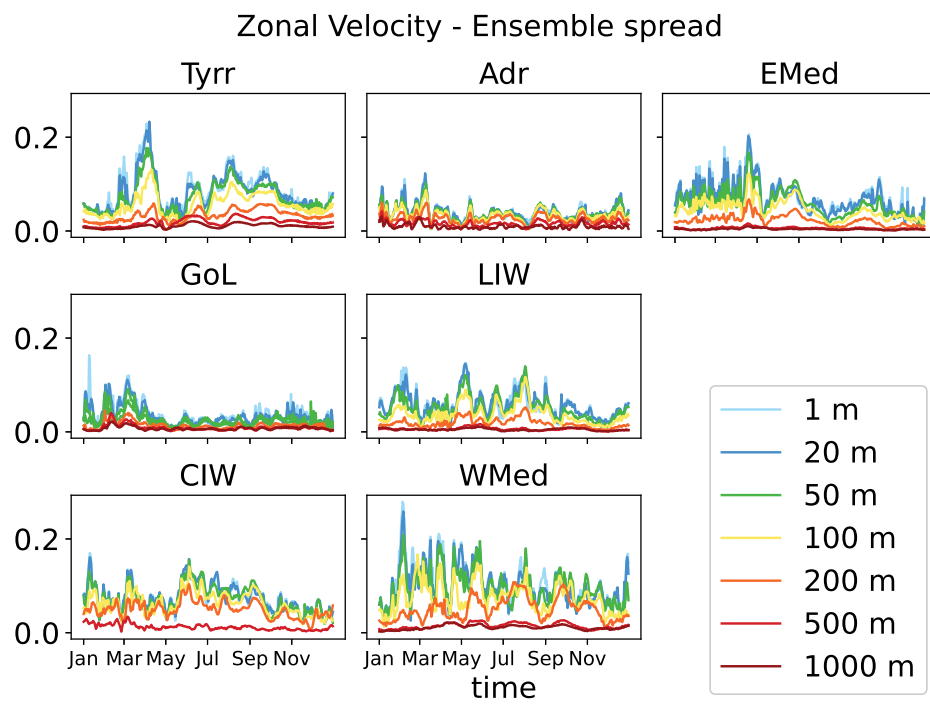


Figure A.8: Time-series of the ensemble spread at the different locations for temperature (top), salinity and zonal velocity (bottom) for seven depth levels.

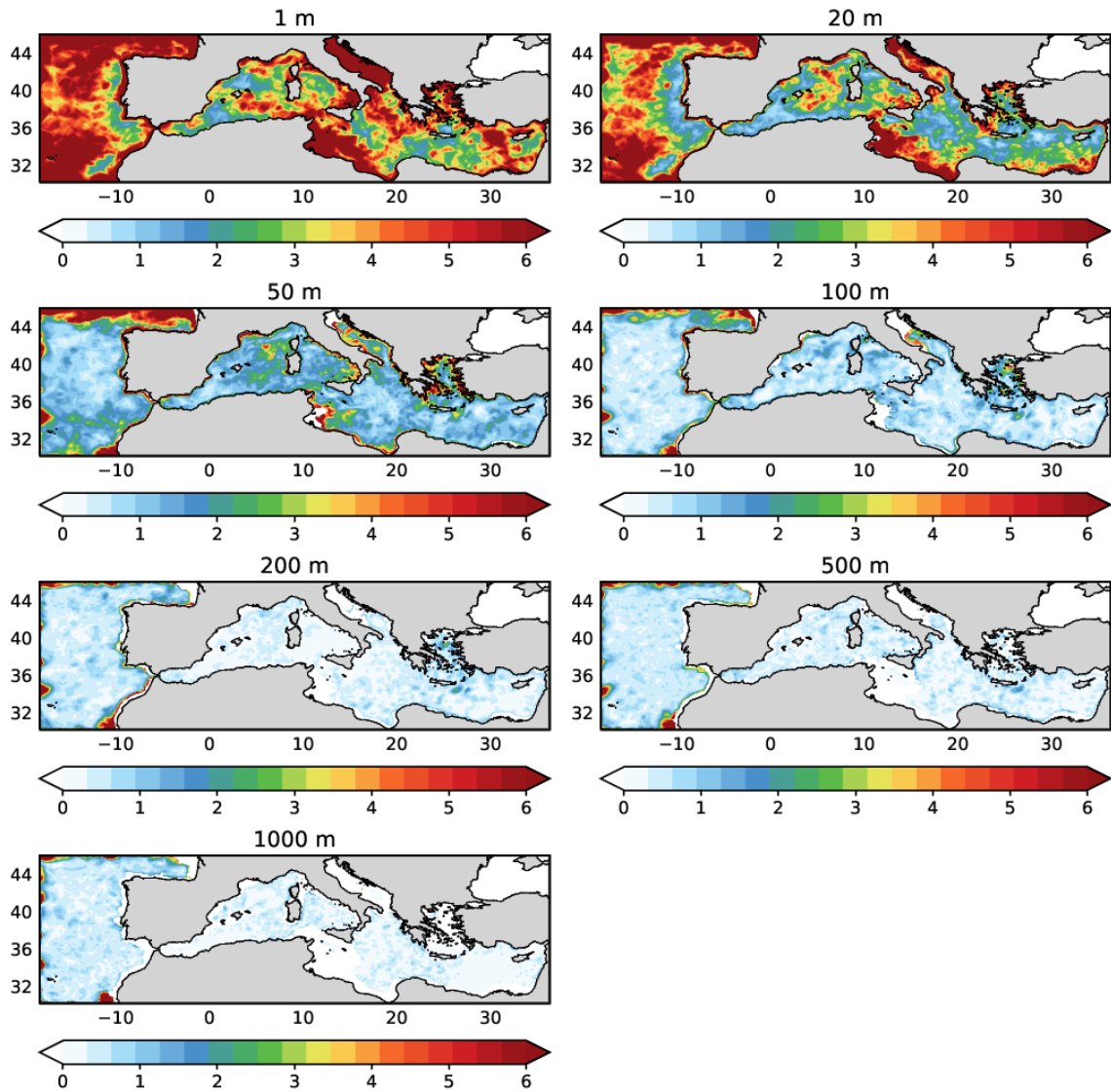


Figure A.9: Signal-to-noise ratio for temperature at different depth levels - JAS

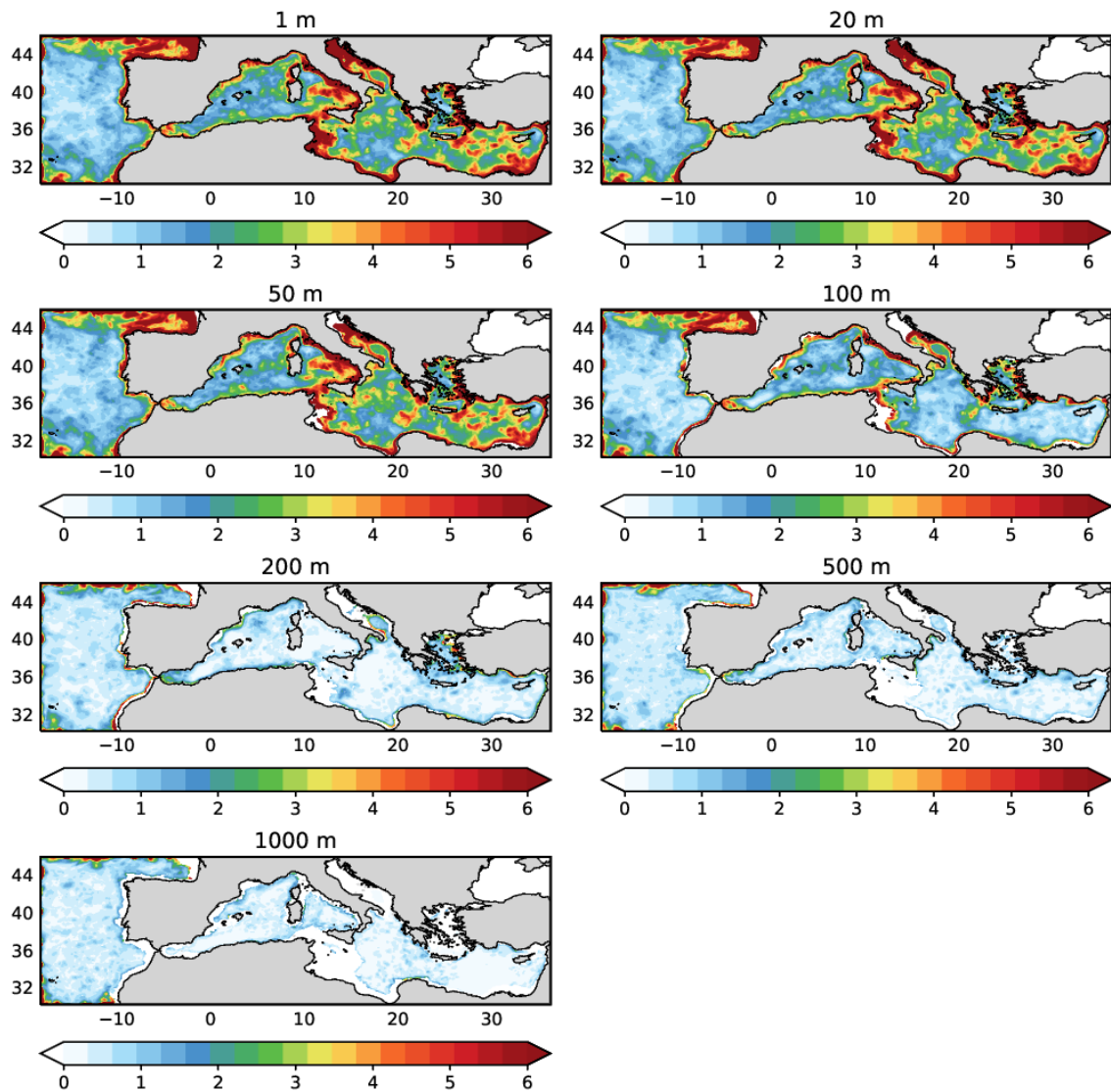


Figure A.10: Signal-to-noise ratio for temperature at different depth levels - JFM

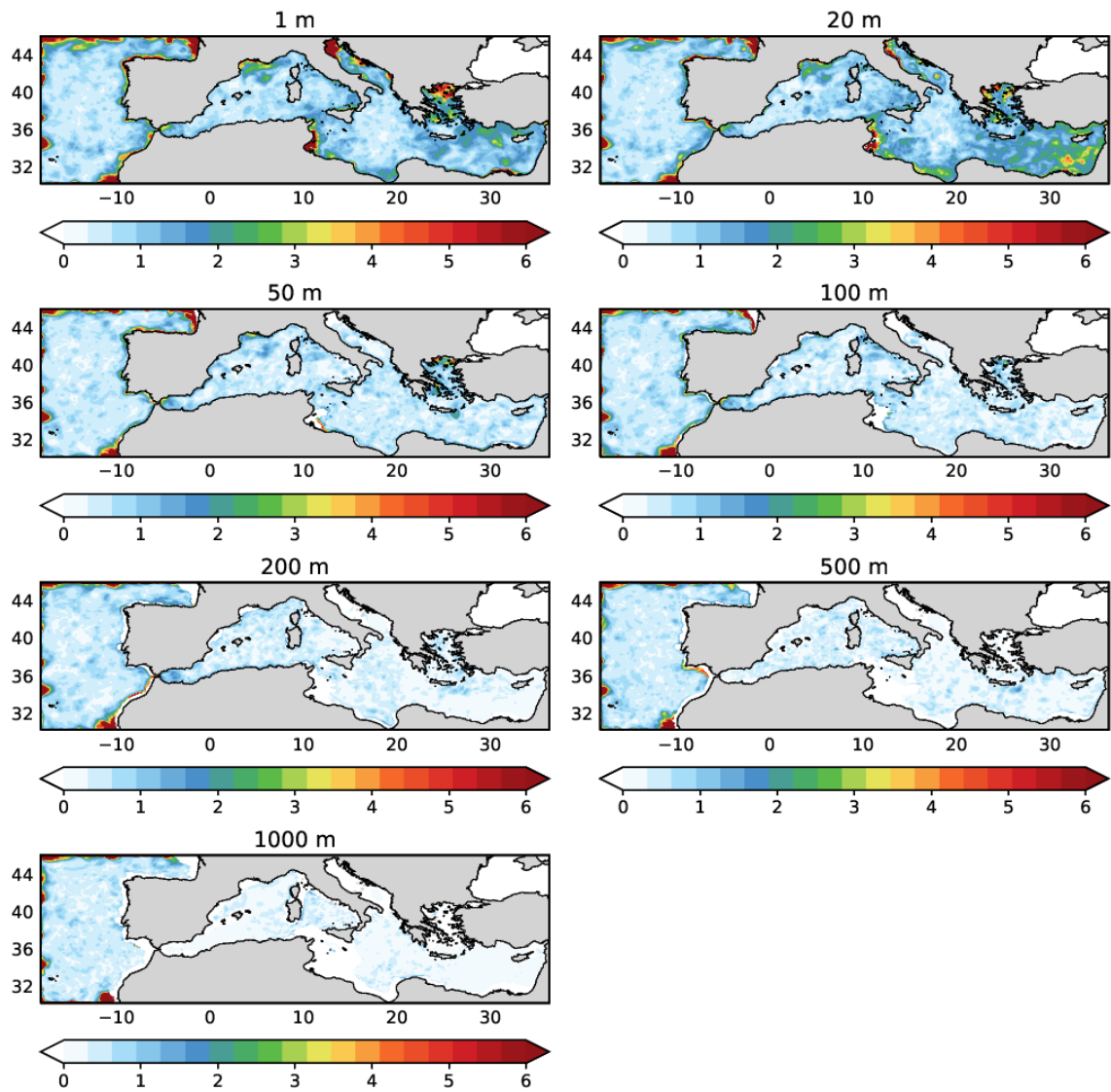


Figure A.11: Signal-to-noise ratio for salinity at different depth levels - JAS

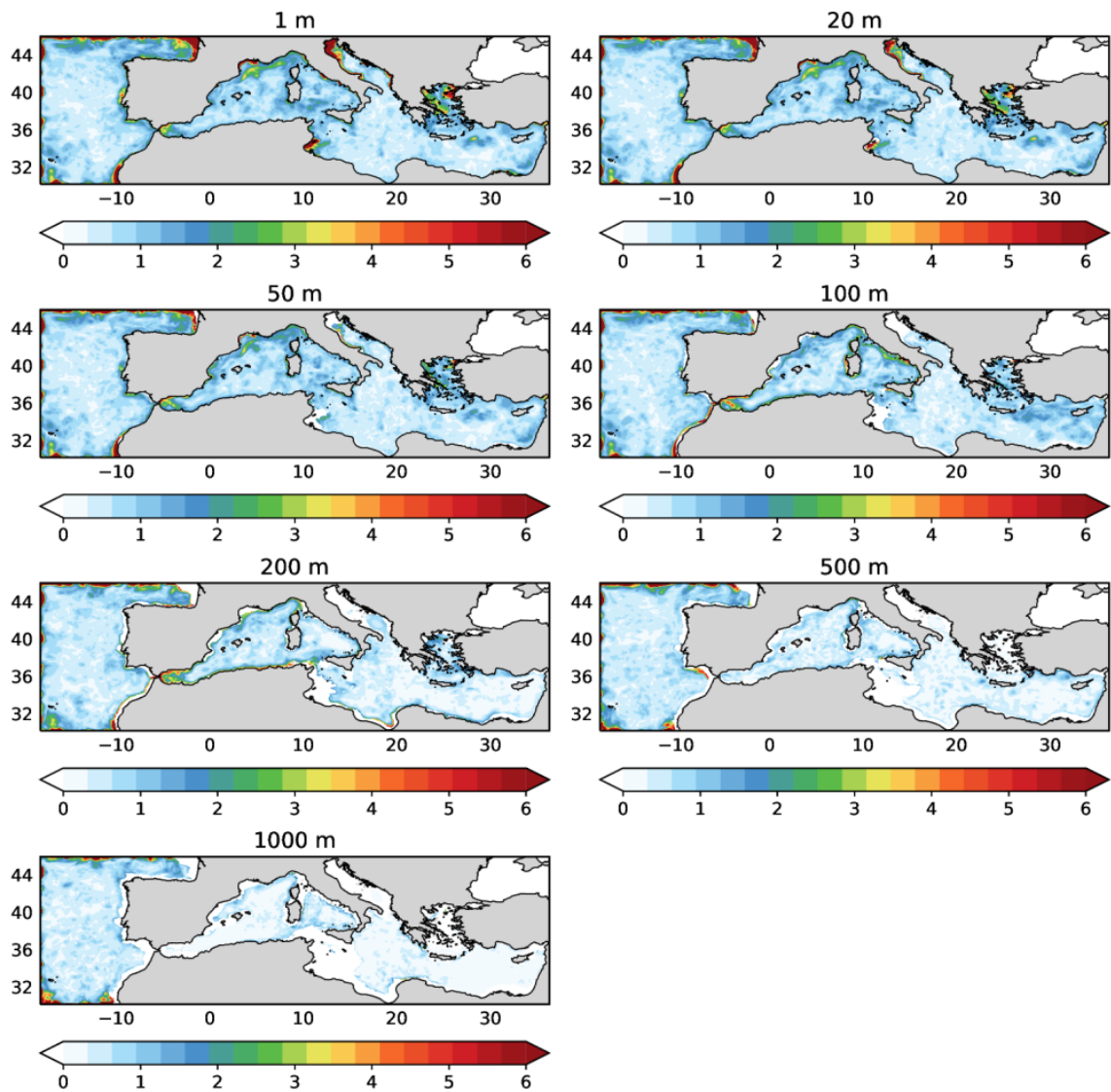


Figure A.12: Signal-to-noise ratio for salinity at different depth levels - JFM

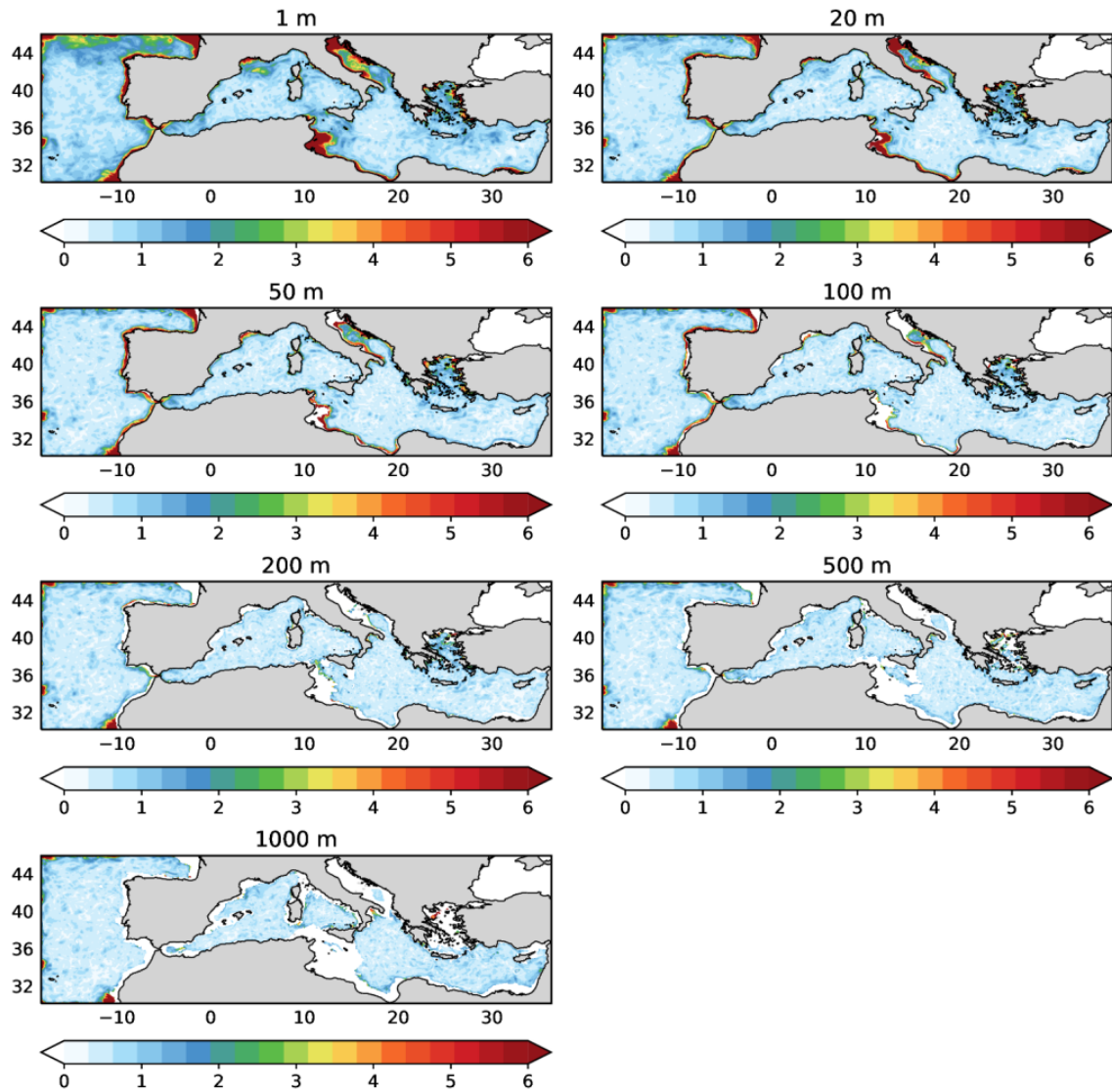


Figure A.13: Signal-to-noise ratio for the current velocity at different depth levels - JAS

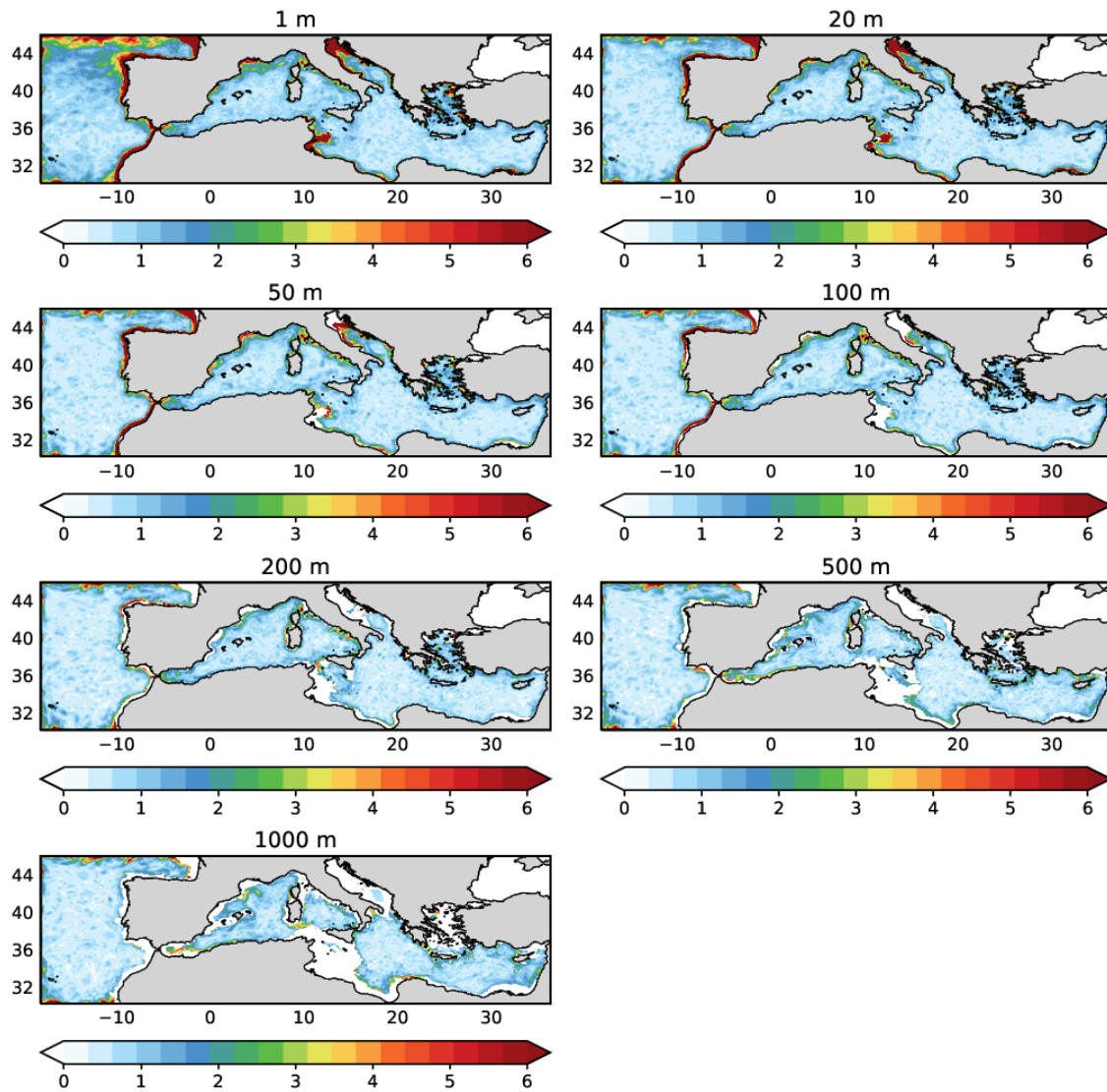


Figure A.14: Signal-to-noise ratio for the current velocity at different depth levels - JFM

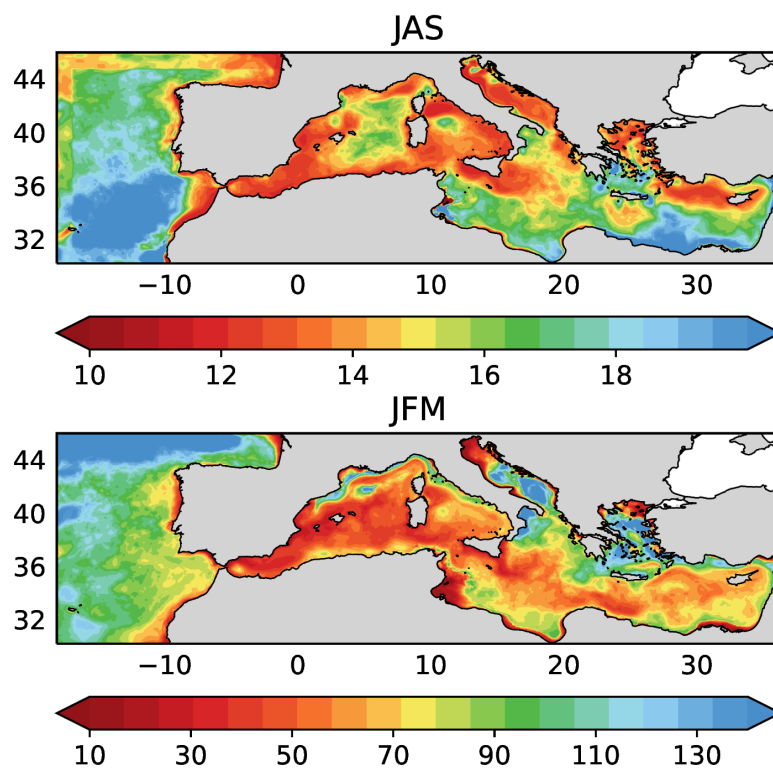


Figure A.15: Seasonal average of the mixed layer depth (m): JAS (top) and JFM (bottom).

BIBLIOGRAPHY

- [1] Storch, Hans von, Jin-Song von Storch, and Peter Müller. "Noise in the climate system—ubiquitous, constitutive and concealing." *Mathematics Unlimited—2001 and Beyond*. Springer, Berlin, Heidelberg, 2001. 1179-1194;
- [2] Hasselmann, Klaus. "Stochastic climate models part I. Theory." *tellus* 28.6 (1976): 473-485;
- [3] Wang, Ming Chen, and George Eugene Uhlenbeck. "On the theory of the Brownian motion II." *Reviews of modern physics* 17.2-3 (1945): 323;
- [4] Franzke, Christian LE, et al. "Stochastic climate theory and modeling." *Wiley Interdisciplinary Reviews: Climate Change* 6.1 (2015): 63-78;
- [5] Palmer, T. N. "Stochastic weather and climate models." *Nature Reviews Physics* 1.7 (2019): 463-471;
- [6] Tang, Shengquan, Hans von Storch, and Xueen Chen. "Atmospherically forced regional ocean simulations of the South China Sea: scale dependency of the signal-to-noise ratio." *Journal of Physical Oceanography* 50.1 (2020): 133-144;
- [7] Williams PD, Haine TWN, Read PL. "On the generation mechanisms of short-scale unbalanced modes in rotating two-layer flows with vertical shear". *J Fluid Mech* 2005, 528:1–22;
- [8] Williams PD, Haine TWN, Read PL. "Inertia–gravity waves emitted from balanced flow: observations, properties, and consequences". *J Atmos Sci* 2008, 65:3543–3556;
- [9] Williams PD, Read PL, Haine TWN. "Spontaneous generation and impact of inertia–gravity waves in a stratified, two-layer shear flow". *Geophys Res Lett* 2003, 30:2255;

BIBLIOGRAPHY

- [10] Williams PD, Haine TWN, Read PL. "Stochastic resonance in a nonlinear model of a rotating, stratified shear flow, with a simple stochastic inertia-gravity wave parameterization". *Nonlin Proc Geophys* 2004a, 11:127–135;
- [11] Lawrence C. Evans, "An introduction to stochastic differential equations. Version 1.2", Department of Mathematics, UC Berkeley;
- [12] Taylor, Geoffrey I. "Diffusion by continuous movements." *Proceedings of the London Mathematical Society* 2.1 (1922): 196-212;
- [13] Uhlenbeck, George E., and Leonard S. Ornstein. "On the theory of the Brownian motion." *Physical Review* 36.5 (1930): 823;
- [14] Frankignoul, Claude, and Klaus Hasselmann. "Stochastic climate models, Part II Application to sea-surface temperature anomalies and thermocline variability." *Tellus* 29.4 (1977): 289-305;
- [15] Hasselmann, Klaus: "On the signal-to-noise problem in atmospheric response studies". *Meteorology over the tropical oceans* (B. D. Shaw, ed.), Royal Met. Soc., Bracknell, Berkshire, England 1979, pp. 251–259;
- [16] Hasselmann Klaus: "Optimal fingerprints for the detection of time dependent climate change". *J. Climate* 6, 1957-1971 (1993);
- [17] Hasselmann, Klaus: "Conventional and Bayesian approach to climate change detection and attribution". *Quart. J. R. Meteor. Soc.* 124, 2541-2565 (1998);
- [18] Clementi, E., Pistoia, J., Escudier, R., Delrosso, D., Drudi, M., Grandi, A., Lecci, R., Cretí, S., Ciliberti, S., Coppini, G., Masina, S., Pinardi, N. (2019). *Mediterranean Sea Analysis and Forecast (CMEMS MED-Currents, EAS5 system) (Version 1) [Data set]*. Copernicus Monitoring Environment Marine Service (CMEMS);
- [19] Pinardi, N., Estournel, C., Cessi, P., Escudier, R., Lyubartsev, V., "Dense and deep water formation processes and Mediterranean overturning circulation", Chapter 7 of "Oceanography of the Mediterranean Sea. An Introductory Guide", edited by Schroeder K. and Chiggiato J., Elsevier, 2023;
- [20] Adani, M., Dobricic, S., Pinardi, N. "Quality assessment of a 1985–2007 Mediterranean Sea reanalysis." *Journal of Atmospheric and Oceanic Technology* 28.4 (2011): 569-589;

BIBLIOGRAPHY

- [21] Pinardi, N., Bonazzi, A., Dobricic, S., Milliff, R. F., Wikle, C. K., Berliner, L. M. (2011). "Ocean ensemble forecasting. Part II: Mediterranean forecast system response." *Quarterly Journal of the Royal Meteorological Society*, 137(657), 879-893;